TRIBHUVAN UNIVERSITY
INSTITUTE OF ENGINEERING
PULCHOWK CAMPUS

DESIGN AND IMPLEMENTATION OF A NICHROME WIRE-BASED RELEASE MECHANISM FOR BALLOON-DEPLOYED FIXED-WING UAV

By:
Anuranjan Nepal (078BAS009)
Arun Panta (078BAS010)
Gyanendra Kumar Shah (078BAS022)
Subash Sapkota (078BAS041)

A FINAL PROJECT REPORT SUBMITTED
TO THE DEPARTMENT OF MECHANICAL AND AEROSPACE ENGINEERING
IN PARTIAL FULFILLMENT OF THE REQUIREMENT FOR THE BACHELOR'S
DEGREE IN AEROSPACE ENGINEERING

DEPARTMENT OF MECHANICAL AND AEROSPACE ENGINEERING
LALITPUR, NEPAL

March, 2026

COPYRIGHT

TRIBHUVAN UNIVERSITY
INSTITUTE OF ENGINEERING
PULCHOWK CAMPUS
DEPARTMENT OF MECHANICAL AND AEROSPACE ENGINEERING

LETTER OF APPROVAL

The undersigned certify that they have read, and recommended to the Institute of Engineering for acceptance, a project report entitled **'DESIGN AND IMPLEMENTATION OF A NICHROME WIRE-BASED RELEASE MECHANISM FOR BALLOON-DEPLOYED FIXED-WING UAV'** submitted by Anuranjan Nepal, Arun Panta, Gyanendra Kumar Shah and Subash Sapkota in partial fulfillment of the requirements for the Bachelor's Degree in Aerospace Engineering.

____

Supervisor : Dr. Hari Bahadur Darlami, Associate Professor
Department of Mechanical and Aerospace Engineering
Institute of Engineering, Pulchowk Campus

____

Supervisor : Er.Biman Rimal, Assistant Professor
Department of Mechanical and Aerospace Engineering
Institute of Engineering, Pulchowk Campus

____

External Examiner : Er.Bibek Dhungana, Assistant Professor
Institute Of Engineering (IOE), Thapathali Campus.

____

Head of Department : Dr. Sudip Bhattrai, Assistant Professor
Department of Mechanical and Aerospace Engineering
Institute of Engineering, Pulchowk Campus

DATE OF APPROVAL : 2083/03/03

ABSTRACT

This study presents the design, fabrication, and experimental validation of a low cost balloon assisted fixed wing UAV system capable of altitude based autonomous deployment and unpowered gliding flight. A lightweight fixed wing glider was developed through four iterative design cycles, yielding a final configuration with a 1.8 m wingspan, 0.27 m^2 wing area, aspect ratio of 12, and an all up mass of 700 g. Preliminary aerodynamic analysis in XFLR5 confirmed static longitudinal stability, while analytical estimation yielded a maximum lift-to-drag ratio of 12.25 and a theoretical minimum sink rate of 0.61 m/s. A nichrome wire burn release mechanism integrated with a SpeedyBee F405 Wing flight controller and MOSFET switching circuit was experimentally verified to provide reliable and repeatable tether severance during bench testing. Deployment validation via a DJI Phantom 4 carrier drone at 43 m and 30m above ground level confirmed stable post-release gliding behavior, with pitch, roll, and yaw all converging to steady-state values following an initial transient disturbance at release. A six balloon latex cluster was analytically determined to provide sufficient buoyant lift under Kathmandu valley atmospheric conditions. This work establishes a replicable proof of concept for autonomous aerial deployment in infrastructure limited environments, with direct relevance to disaster reconnaissance and remote payload delivery across Nepal's Himalayan terrain.

Keywords: Autonomous Deployment, Balloon-Launched Glider, XFLR5, Nichrome Wire Burn, SpeedyBee F405, MOSFET, Reconnaissance

ACKNOWLEDGEMENT

We would like to express our sincere gratitude to the Department of Mechanical and Aerospace Engineering, Institute of Engineering, Pulchowk Campus, for providing us with the opportunity, resources, and academic environment necessary to undertake and successfully complete this major project.

We are deeply thankful to our project supervisors, **Assoc. Prof. Hari Bahadur Darlami** and **Asst. Prof. Biman Rimal**, for their continuous guidance, constructive feedback, and unwavering encouragement throughout the course of this project. Their technical insights, inspiring lectures, and consistent support were invaluable in shaping the direction and successful completion of our work.

We would also like to extend our sincere appreciation to all faculty members of the Department of Mechanical and Aerospace Engineering whose academic teachings over the past four years provided the foundational knowledge that made this project possible. This project has greatly enriched our understanding and provided us with a meaningful experience of collaborative engineering work. We are equally grateful to our friends and colleagues who contributed directly and indirectly at various stages of this project. Their support, suggestions, and cooperation are sincerely acknowledged.

Finally, we place a deep sense of appreciation towards our families, whose constant encouragement, patience, and moral support remained a source of inspiration throughout this journey.

Any suggestions or constructive criticism regarding this work are most welcome and will be gratefully acknowledged.

Authors:
Anuranjan Nepal
Arun Panta
Gyanendra Kumar Shah
Subash Sapkota

TABLE OF CONTENTS

LIST OF FIGURES

LIST OF TABLES

LIST OF ABBREVIATION

BOM	Bill of Materials
CAD	Computer-Aided Design
CG	Center of Gravity
EKF	Extended Kalman Filter
EO	Electro-Optical
ESC	Electronic Speed Controller
GPS	Global Positioning System
GCS	Ground control station
HAB	High-Altitude Balloon
HIL	Hardware-in-loop
IMU	Inertial Measurement Unit
IR	Infrared
LiPo	Lithium Polymer
NP	Neutral Point
PDB	Power Distribution Board
RC	Radio Control
UAV	Unmanned Aerial Vehicle

LIST OF SYMBOLS

Symbol	Description	Unit
F_D	Drag force	N (Newton)
Δz	Vertical displacement	m (meter)
ρ	Density of air	kg/m^3
A	Reference area (e.g., parachute or balloon)	m^2
v	Velocity	m/s
C_D	Drag coefficient	Dimensionless
m	Mass (general)	kg
g	Gravitational acceleration	m/s^2
v_T	Terminal velocity	m/s
P	Pressure	Pa (Pascal)
V	Volume	m^3
n	Number of moles of gas	mol
R	Universal gas constant (8.31 J/(mol·K))	J/(mol·K)
T	Temperature	K (Kelvin)
M_a	Average molecular mass of air (28.97 kg/mol)	kg/mol
ρ_a	Density of air	kg/m^3
P_a	Atmospheric pressure	Pa
T_a	Atmospheric temperature	K
V_b	Balloon volume	m^3
m_g	Mass of fill gas	kg
T_g	Fill gas temperature	K
M_g	Molecular mass of fill gas	kg/mol
P_g	Fill gas pressure	Pa
r	Balloon radius	m
D	Diameter of balloon	m
ρ_s	Lifting gas density	kg/m^3
m_B	Mass of balloon system	kg
m_p	Payload mass	kg
F_L	Lifting force	N

CHAPTER ONE:
INTRODUCTION

1.1 Background

Unmanned Aerial Vehicles (UAVs) have experienced rapid growth in recent decades owing to their operational versatility, relatively low cost, and ability to perform missions in environments that are hazardous or inaccessible to human operators. UAVs are now extensively employed across a wide range of civilian and scientific applications, including aerial surveillance, environmental monitoring, disaster response, precision agriculture, communication relay, and topographic mapping.

Despite these advances, conventional UAV operations continue to face fundamental limitations in mountainous terrain, remote regions, and high-altitude environments, where dedicated takeoff and landing infrastructure is unavailable, terrain is highly irregular, and physical access to deployment sites is severely restricted. These challenges are of particular relevance in Nepal, a country characterised by extreme topographic diversity, ranging from the Terai plains to some of the world's highest mountain peaks. Nepal is also among the most disaster prone nations in the world, regularly affected by earthquakes, flash floods, landslides, and avalanches. In the aftermath of such events, rapid aerial reconnaissance and payload delivery to affected communities can be critical to saving lives.However, the same terrain features that make Nepal geographically unique also make it among the most difficult environments in the world for conventional UAV deployment. Ground launched systems are constrained by their limited altitude ceiling relative to surrounding terrain, while helicopter based operations are expensive and often impractical in remote areas. Therefore, there exists a strong practical motivation for the development of alternative aerial deployment strategies suited to Nepal's geographic and operational context.

One promising approach to overcoming these limitations is the balloon deployed UAV concept, in which a light weight fixed wing UAV is carried to a desired altitude by a lighter than air platform, typically a gas filled balloon and subsequently released to transition into controlled gliding flight. Unlike conventional runway launched or hand launched UAV systems, balloon assisted deployment can significantly increase the effective starting altitude of the aircraft, thereby extending its operational range and enabling deployment over terrain where direct launch would be impossible. This concept is especially suited to high altitude and mountainous applications, as the balloon provides buoyancy driven ascent with minimal energy expenditure from the UAV itself, effectively decoupling the vertical and horizontal components of the mission profile. Balloon assisted aerial deployment has previously been explored in the context of high altitude atmospheric research, stratospheric glider recovery, emergency payload delivery, and long range remote sensing, where the combination of buoyancy based ascent and aerodynamic glide provides a simple yet energy efficient mission architecture. In such systems, the balloon serves as a passive vertical lift mechanism while the UAV provides horizontal mobility, navigational control, and mission adaptability following release. This hybrid approach is particularly advantageous for terrain independent launch capability, wide area coverage from altitude, and payload delivery to inaccessible zones, all of which are directly relevant to operational requirements in Nepal's mountain and hill regions.For a balloon deployed UAV system to function reliably, several interconnected engineering challenges must be addressed. These include the design of a lightweight yet aerodynamically stable fixed wing glider platform, the development of a reliable and repeatable aerial release mechanism, the integration of flight control electronics and autonomous navigation systems, and the selection of a suitable balloon material and lifting gas capable of generating sufficient buoyant force under local atmospheric conditions. At higher altitudes, additional factors such as reduced air density, altered aerodynamic characteristics, wind drift, and low-temperature effects on electronics and materials must also be considered. A successful balloon deployed UAV therefore requires a multidisciplinary approach encompassing aerodynamics, structural design, electronics integration, and lighter-than-air system engineering.

This project was undertaken to investigate the feasibility of developing a low-cost, lightweight, and modular balloon deployed fixed wing UAV prototype suitable for future high altitude and remote area deployment missions. The study encompasses the aerodynamic design and physical fabrication of a glider based UAV platform, the development and testing of a nichrome wire burn wire aerial release mechanism, and the evaluation of flight performance through analytical estimation, XFLR5 simulation, and physical drop tests. During the course of development, practical limitations of an initial custom-fabricated polyethylene balloon envelope specifically recurring gas leakage at seam regions necessitated a transition to a commercial latex balloon solution, reflecting the real engineering challenges involved in transforming a conceptual deployment system into a field-ready prototype.

The significance of this study lies in its exploration of an alternative UAV deployment methodology that is directly relevant to remote, high altitude, and infrastructure limited environments. By combining the passive vertical lift capability of a gas balloon with the aerodynamic gliding efficiency of a fixed wing airframe, this project aims to establish a foundational proof of concept for a system capable of supporting applications such as disaster reconnaissance, remote sensing, environmental monitoring, and payload delivery in challenging Himalayan terrain. The work also contributes to the broader objective of developing locally adaptable, low cost aerospace solutions for real world operational challenges in Nepal and comparable geographic regions.

1.2 Problem Statement

Aerial operations in Nepal's mountainous and remote regions are severely constrained by difficult terrain, poor ground accessibility, absence of launch infrastructure, and high operational costs associated with conventional aerial platforms. Ground launched UAVs are limited in their ability to achieve sufficient altitude for wide area coverage over rugged topography, while helicopter based operations are prohibitively expensive for routine deployment. Existing balloon based systems, although capable of reaching high altitudes, have historically lacked reliable and precisely controlled release mechanisms for fixed wing UAV deployment, limiting their practical utility.

Furthermore, the absence of integrated systems that ensure stable aerodynamic transition following release, controlled gliding flight, and safe descent restricts the practical implementation of balloon UAV hybrid concepts. Local availability of suitable components, including weather grade balloon envelopes and precision electronics, presents an additional constraint for low cost system development in Nepal. There is therefore a clear need for a low cost, reliable, and locally realisable aerial deployment system capable of altitude based autonomous release, stable post deployment gliding flight, and controlled descent in remote and mountainous environments.

1.3 Objectives

The main objective of the study is to design, develop, and experimentally validate a low cost balloon assisted aerial deployment system for a fixed wing glider UAV, ensuring reliable release, stable post-deployment behavior, and controlled descent under low altitude conditions.
The specific objectives are:

- To design and fabricate a lightweight fixed wing glider optimized for stable unpowered flight.
- To develop a reliable nichrome wire burn release mechanism for aerial deployment.
- To integrate avionics, control systems, and the release mechanism using a unified onboard power system.
- To perform intermediate deployment testing via drone before transitioning to balloon based deployment.
- To analyze flight stability through key parameters:pitch, roll, yaw, and altitude variation over time.

1.4 System Used

1.4.1 Hardware used

The hardware components required for the project are listed below:

1. **Aerial Platform:** Foam-based fixed wing glider structure with control surfaces (ailerons and elevator), designed for low speed gliding flight.

2. **Avionics System:** SpeedyBee F405 Wing flight controller with integrated IMU, barometer, and support for GPS modules.

3. **Power System:** 3S LiPo battery used to power avionics, servos, and the release mechanism.

4. **Deployment System:** Latex/weather balloon and nichrome wire burn mechanism with MOSFET-based current control for payload release.

5. **Control System:** RC transmitter receiver setup for manual control, testing, and fail safe operation.

6. **Actuation System:** Three servos (two for ailerons and one for elevator control).

7. **Intermediate Test Platform:** Multirotor UAV (drone) used for controlled low altitude deployment testing prior to balloon based deployment.

1.4.2 Software Used

The software tools required for the project are listed below:

1. **Autopilot Firmware:** ArduPilot firmware for flight stabilization and control.

2. **Ground Control Station (GCS):** Mission Planner or QGroundControl for flight configuration and monitoring.

3. **Aerodynamic Analysis:** XFLR5 for preliminary aerodynamic design and stability analysis.

4. **CAD Design Software:** CATIA for structural design and component modeling.

5. **Flight Simulation:** X-Plane for preliminary flight behavior validation.

6. **Balloon Analysis Tools:** Totex Balloon Burst Estimator and Stratoflights for payload and trajectory estimation.

7. **Flight Controller Configuration:** SpeedyBee Configurator for calibration, sensor setup, and system tuning.

CHAPTER TWO:
LITERATURE REVIEW

2.1 High Altitude Balloon for Scientific and Survelliance Application

High-altitude balloons (HABs) have long served as cost-effective and reliable platforms for carrying scientific payloads to the stratosphere, operating at altitudes between 20 and 40 km above sea level. Their ability to carry multi-kilogram payloads to near-space environments at a fraction of the cost of orbital or sub-orbital launch vehicles has made them a popular tool for atmospheric research, remote sensing, and instrument testing under real stratospheric conditions [1].The DLR HABLEG project demonstrated the deployment of a small glider from a stratospheric balloon at approximately 20 km altitude, validating aerodynamic perfor mance and control law behaviour under stratospheric conditions [1]

Beyond atmospheric science, HABs are increasingly employed as deployment vehicles for unmanned aerial vehicles (UAVs). The balloon-launched UAV concept exploits the proven altitude capability of HABs to place a small glider or powered UAV at stratospheric altitude, from which it is released for controlled flight. This approach eliminates the need for onboard propulsion during the ascent phase, reducing structural mass and energy requirements compared to a self-powered climb [1]. The technique also provides a controlled and repeatable way to test aerodynamics, avionics, and control systems under real low-density, low-Reynolds-number conditions that cannot easily be replicated in ground-based facilities [1], [3].

A HAB system typically consists of a latex or zero-pressure polyethylene envelope filled with helium or hydrogen, a payload gondola, a parachute recovery system, and a flight computer for telemetry and tracking. The balloon ascends at a controlled rate until the envelope bursts at altitude due to reduced ambient pressure, after which the payload descends under a parachute for recovery. Mission planning therefore requires accurate trajectory prediction to ensure the payload lands within a recoverable zone [2].

Smith [2] presented a high-altitude balloon trajectory optimisation methodology for enhanced mission planning and multi-platform system integration. The study developed a trajectory predictor using simplified first-order equations governing ascent, float, and descent phases, with horizontal motion modelled via NOAA GFS wind data. An in-flight objective trajectory generation method allowed optimisation of launch location and timing to achieve a desired position, altitude, and time-of-arrival. Validation against actual latex balloon flights reduced landing prediction error from 6 km to under 1 km, and the approach was demonstrated in NASA Space Grant's Nationwide Eclipse Ballooning Project, confirming its applicability to real-world missions [2].

NASA's ARES project employed drop tests from high-altitude balloons to model subscale flights in low-density environments, demonstrating the broader applicability of the balloon-launch paradigm across different mission contexts [4]. These precedents establish HAB-launched UAV deployment as a mature and well-validated technique for stratospheric and near-space experimentation.

2.2 Fixed wing UAVs for long endurance remote sensing

Aerodynamically optimised airframes reduce parasitic drag and energy consumption, while autopilot systems enable fully autonomous navigation [3]. Structural components employ lightweight composite materials with impact-resistant sections to improve durability, and modular payload bays with reconfigurable avionics allow multi-mission adaptability [4]. Long-Endurance Electric UAVs (LEEUAVs) fixed-wing unmanned aircraft designed to maximise flight duration using electric propulsion — have attracted significant research interest for remote sensing and surveillance applications. Recent LEEUAV designs focus on extended endurance through the use of high-capacity battery packs, often supplemented by solar energy harvesting integrated into the wing surface [5].

A solar-assisted electric UAV was developed using both low-fidelity internal design tools and commercial high-fidelity software, with lightweight materials and efficient structural techniques improving aerodynamic and propulsion performance [4]. Initial prototype tests validated handling and flight characteristics, and a more rigid wing was subsequently constructed for structural validation and integration with future UAV systems [1]. This iterative design-and-test methodology is representative of current best practice in academic UAV development programmes.

LEEUAVs achieve low-power, long-duration flight through the combination of lightweight airframes and optimised aerodynamic configurations. Reported performance figures for representative LEEUAV platforms include short ground takeoff distances of approximately 8 m, or 3 m when hand-launched; a rapid climb to 1,000 m within 10 minutes; sustained cruise at speeds above 7 m/s for up to 8 hours; and a 29-minute gliding descent to a field landing [5]. These performance characteristics reflect the importance of low wing loading and high lift-to-drag ratios in long-endurance design.

For Beyond Visual Line of Sight (BVLOS) operations, LEEUAVs are commonly equipped with a First Person View (FPV) system comprising an airborne video transmitter and a Ground Control Station (GCS). The GCS receives real-time video via a 1.3 GHz analogue receiver displayed on a high-brightness LCD monitor. Antenna selection is matched to operational range: skew planar wheel antennas are used for short-range missions, while 11 dBi heliaxial antennas are employed for long-range BVLOS sorties [3][5].

2.3 High-Altitude Balloon-Launched UAV and Glider Systems

High-altitude UAVs attract increasing interest due to their potential to operate in the stratosphere, enabling surveillance, communication relay, and scientific measurement missions that are impractical with conventional lower-altitude platforms. Traditional High-Altitude Long-Endurance (HALE) platforms such as NASA's Pathfinder, Helios, and QinetiQ Zephyr demonstrated the feasibility of very long-endurance stratospheric flight, but required large, structurally fragile airframes with complex propulsion systems that limit accessibility and increase cost [1][6].

The concept of a balloon-launched UAV eliminates onboard propulsion during ascent and offers a cost-effective and flexible means of conducting short-duration experiments at high altitudes [6]. The DLR HABLEG project presents a well-documented example of stratospheric balloon-assisted deployment, achieving release altitudes of approximately 20 km above ground level, at which aerodynamic and control system testing could be performed under real stratospheric conditions [6].

Balloon-launch systems utilise the proven technology of high-altitude balloons to deliver small gliders or UAVs to altitude with less energy expenditure and fewer structural constraints than a self-powered ascent [10]. NASA's ARES project similarly employed balloon drop tests to model sub-scale flights in low-density environments [4][6]. To maintain favourable stability and control under the low-Reynolds-number conditions encountered at high altitude, the HORUS glider configuration employed a relatively low-aspect-ratio wing (AR 3.6) together with all-moving horizontal and vertical tail surfaces [6]. The HORUS platform was developed as a balloon-launched high-altitude glider to provide controlled recovery of atmospheric sampling payloads, improving the operational flexibility of conventional AirCore systems [7].

Among the most challenging manoeuvres in a balloon-launched UAV mission is transitioning from vertical free-fall to horizontal stable flight. This process involves a rapid change in flight regime including attitude, airspeed, and aerodynamic force distribution [9]. In HABLEG, a cascaded PID controller was used alongside a collection of discrete flight modes to govern ascent, release, transition, and glide phases. Real flight data revealed that gain scheduling based on dynamic pressure can produce instability at high true airspeeds encountered during the initial altitude flight phase, highlighting the need for robust control law design [12].

Mission simulation and hardware-in-the-loop (HIL) testing have been demonstrated as essential risk-reduction tools for high-altitude UAV missions [8]. During the HABLEG project, partial HIL simulation significantly enhanced mission crew readiness, and post-flight analysis identified control oscillations and sensor performance anomalies during the transition and glide phases [8]. Redundant GPS receivers and dual telemetry links further ensured navigational integrity throughout the mission, confirming the effectiveness of sensor redundancy strategies for high-altitude operations [13], [14].

Unlike the HABLEG project, which employed a cascaded PID controller with dynamic-pressure-based gain scheduling and a dedicated multi-mode flight management system to handle the vertical-to-horizontal transition, the present project adopts a simpler fixed-gain control architecture combined with conservative release-altitude and glide-angle selection[7][9]. This choice is motivated by the lower deployment altitude (approximately 30 km versus HABLEG's 20 km) and the more benign aerodynamic environment at the targeted release conditions, which reduces the severity of the transition manoeuvre and allows a less complex control solution to be used without compromising mission safety.[15]

CHAPTER THREE: METHODOLOGY

3.1 Introduction

In the flowchart, the step-by-step progress of the team is outlined. It all begins with the definition of the problem statement, followed by a literature review to gain a thorough understanding of the subject. After this, the team works in parallel to build the UAV, build and test the balloon filled with hydrogen, and build and test the release mechanism.

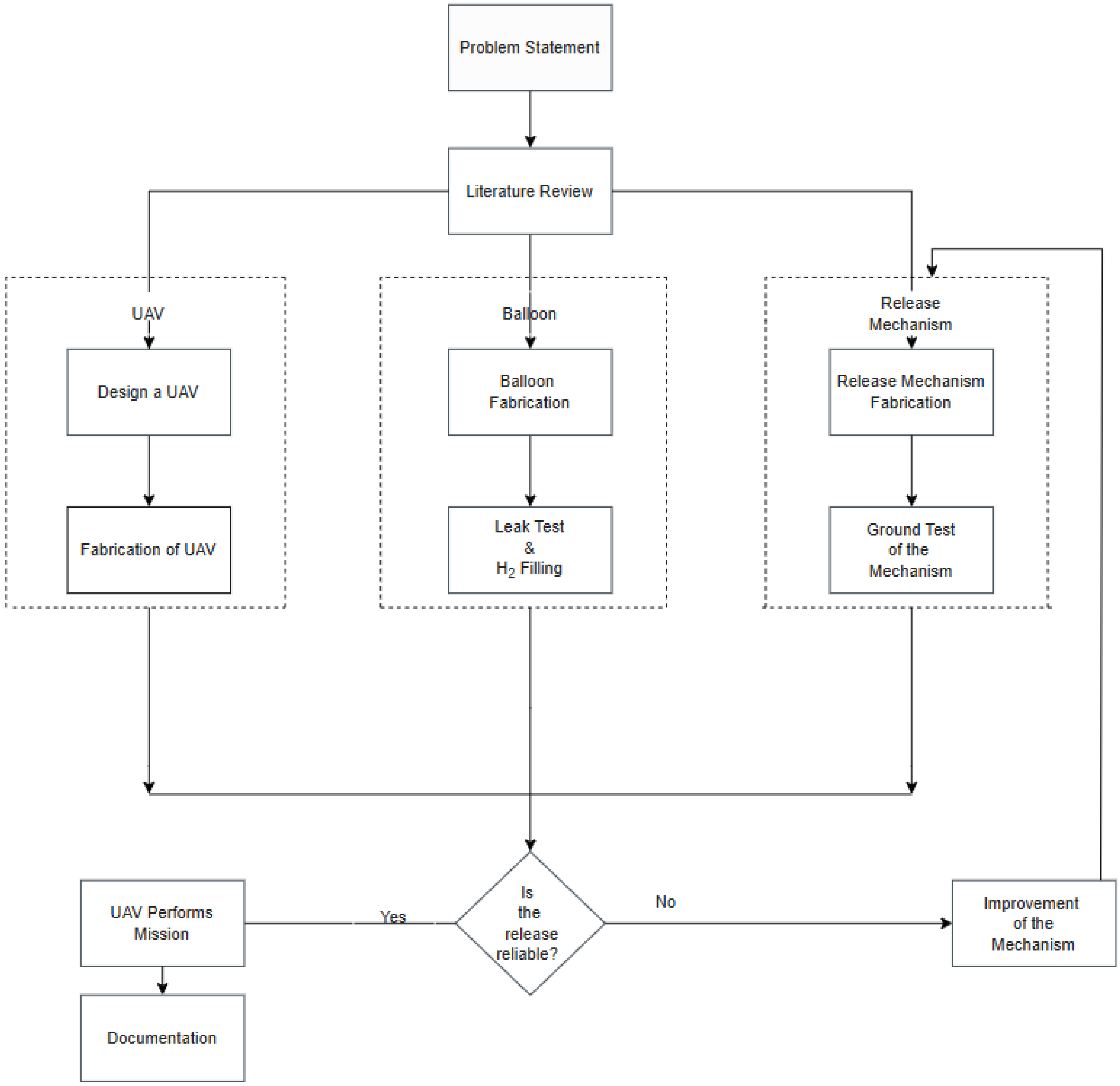

Figure 3.1: Flow Chart

3.2 System Design and Development Plan

3.2.1 Overall System Architecture

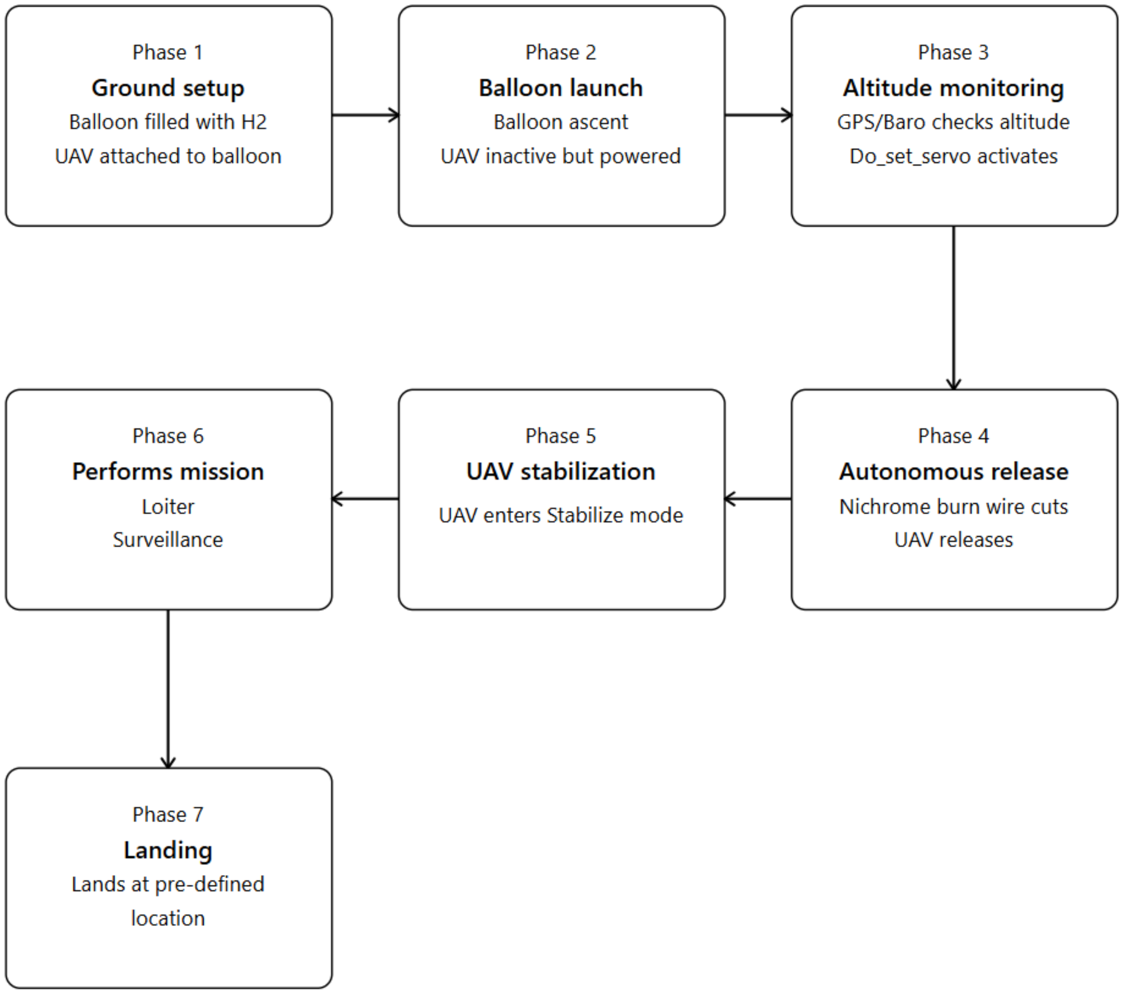

Figure 3.2: System Architecture

3.3 Theoretical Background

3.3.1 High-Altitude Balloon Flight Dynamics

The total lifting capability of a high-altitude balloon is determined by the buoyant force generated by the lifting gas, which depends fundamentally on the density difference between the filling gas and the surrounding atmospheric air. Under standard atmospheric conditions at sea level, air has a density of approximately 1.225 kg/m³. Hydrogen, with a density of approximately 0.09 kg/m³, provides a net lifting capability of roughly 1.1 kg per cubic metre of gas volume, while helium, with a higher density of approximately 0.17 kg/m³, generates a slightly lower net lift of around 1.0 kg per cubic metre.

The gross lift produced by the balloon is calculated from the total enclosed gas volume multiplied by the effective density difference between displaced air and the lifting gas. From this gross lift, the combined mass of the balloon envelope and the suspended

payload must be subtracted to obtain the free lift. Free lift is a critical operational parameter as it directly governs the balloon's ascent rate and altitude profile.
For typical experimental balloon flights, a recommended free lift is selected to achieve a controlled ascent rate of approximately 320 m/min (1000 ft/min). Increasing the payload mass beyond the nominal design value results in a reduced ascent rate, a lower burst altitude, or both. Computational tools such as the Totex Balloon Burst Estimator were used in this project to evaluate the relationship between balloon size, payload mass, launch diameter, ascent rate, and expected burst altitude.

3.3.1.1 Basic Forces and Lift

In a stationary atmosphere, where there are no vertical winds, a high-altitude balloon experiences a set of vertical forces that determine its ascent and equilibrium. The principal upward force acting on the balloon is the buoyant force, often referred to as the gross lift. This force arises from the displacement of atmospheric air by the lighter-than-air gas within the balloon. Mathematically, the gross lift F_B is given by:

$$F_B = (m_a - m_g) \cdot g \tag{3.1}$$

where:

- m_a is the mass of atmospheric air displaced by the gas volume (equivalent to the mass of the same volume of air),
- m_g is the mass of the lifting gas (such as hydrogen or helium), and
- $g = 9.8\,\text{m/s}^2$ is the acceleration due to gravity.

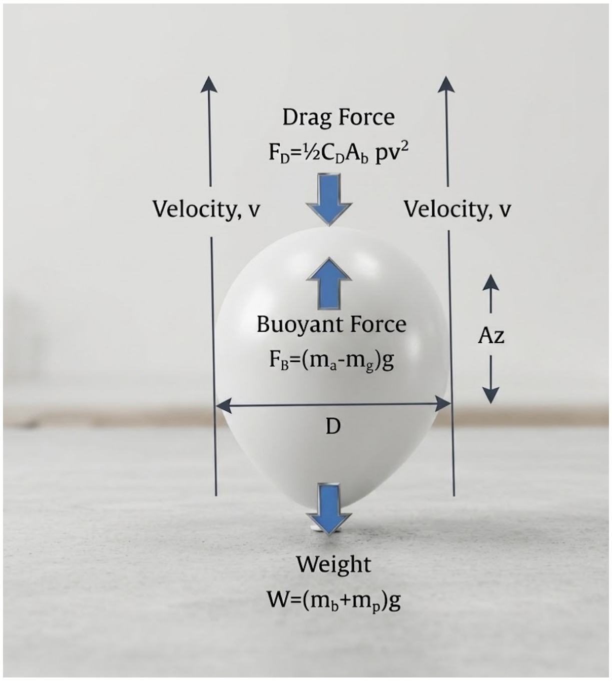

Figure 3.3: Balloon Dynamics

At standard temperature and pressure (STP), hydrogen has a density of approximately $0.09\,\text{kg/m}^3$, while air has a density of about $1.2\,\text{kg/m}^3$, resulting in a net lifting capability of roughly $1.1\,\text{kg/m}^3$ of hydrogen.

The total mass suspended below the balloon, called the gross mass m_a, includes both the mass of the balloon envelope itself m_b and the mass of the payload m_p, such that:

$$m_a = m_b + m_p \tag{3.2}$$

From the gross lift, two other important quantities can be derived. The nozzle lift is the lifting force when only the balloon is attached (without payload), and it is given by:

$$F_n = F_B - m_b \cdot g \tag{3.3}$$

The free lift, which is the net lift available after accounting for both the balloon and the payload, is:

$$F_L = F_B - W = F_B - m_a \cdot g \tag{3.4}$$

where W is the total weight of the balloon system.
Free lift is the quantity that governs the balloon's initial rate of ascent and is a critical parameter for determining the altitude profile during flight.

3.3.1.2 Drag Force

When the balloon system is first launched, it quickly accelerates to a constant upward speed based on the force balance between the free lift force and the drag force:

$$F_L = F_D \tag{3.5}$$

The drag force is given by:

$$F_D = \frac{1}{2} C_D A_b \rho v^2 \tag{3.6}$$

where:

- $A_b = \frac{\pi D^2}{4}$ is the cross-sectional area of the balloon (with D being the balloon diameter),
- ρ is the atmospheric air density,
- v is the upward velocity of the balloon,
- C_D is the drag coefficient, typically about 0.3

To understand this relationship, the principle of conservation of energy can be used.
The work done by the drag force when the balloon ascends a vertical increment Δz is:

$$W = F_D \cdot \Delta z \tag{3.7}$$

This is proportional to the kinetic energy imparted to the displaced air:

$$W = \frac{1}{2} m v^2 \tag{3.8}$$

where the mass of displaced air is:

$$m = \rho V = \rho A \cdot \Delta z$$

Substituting this into the kinetic energy expression:

$$F_D \cdot \Delta z \propto \frac{1}{2}\rho A \cdot \Delta z \cdot v^2 \tag{3.9}$$

$$\Rightarrow F_D = \frac{1}{2}C_D A_b \rho v^2 \tag{3.10}$$

confirming equation 3.6.

This same formula applies to the analysis of parachute descent by taking A_p as the area of the parachute. At terminal descent velocity v_T, the drag force equals the system's weight:

$$mg = F_D = \frac{1}{2}C_D A_p \rho v_T^2 \tag{3.11}$$

Solving for the terminal velocity v_T gives:

$$v_T = \sqrt{\frac{2mg}{C_D A_p \rho}} \tag{3.12}$$

3.3.1.3 Gas Law Equations

For an ideal gas, the equation of state is given by:

$$PV = nRT \tag{3.13}$$

where:

P = pressure (Pa)
V = balloon volume (m^3)
n = number of moles of lifting gas (mol)
R = 8.31 J/(mol·K), universal gas constant
T = internal balloon temperature (K)

If we multiply both sides of this equation by the average molecular mass of air M_a = 28.97 kg/mol, we obtain an expression for the density of air:

$$\rho_a = \frac{M_a P_a}{R T_a} \tag{3.14}$$

where:

ρ_a = density of air (kg/m^3)
P_a = atmospheric pressure (Pa)
T_a = atmospheric temperature (K)

We can also solve for the volume of the balloon using the fill gas parameters (denoted with the subscript g):

$$V_b = \frac{m_g R T_g}{M_g P_g} \tag{3.15}$$

where:

$$V_b = \text{balloon volume (m}^3\text{)}$$
$$m_g = \text{mass of fill gas (kg)}$$
$$T_g = \text{fill gas temperature (K)}$$
$$M_g = \text{molecular mass of fill gas (kg/mol)}$$
$$P_g = \text{fill gas pressure (Pa)}$$

When the balloon is approximated as a sphere, the volume is:

$$V_b = \frac{4}{3}\pi r^3 \tag{3.16}$$

where r is the balloon radius (m).

3.3.1.4 Equations of Motion

By applying Newton's Second Law, $F = ma$, the dynamic motion of the balloon can be analyzed using a second-order differential equation with certain approximations (Bachman).
At steady state, where acceleration $a = 0$, the net force is zero, and the upward lifting force is exactly balanced by the drag and weight forces:

$$F_L = F_D \tag{3.17}$$

The steady-state ascent velocity v can be derived from the force balance and is given by:

$$v = \sqrt{\frac{\left(\frac{\pi D^3}{6}(\rho - \rho_s)g - (m_B + m_p)g\right)}{\left(\frac{C_D \rho \pi D^2}{8}\right)}} \tag{3.18}$$

where:

$$D : \text{Diameter of the balloon (m)}$$
$$\rho : \text{Atmospheric air density (kg/m}^3\text{)}$$
$$\rho_s : \text{Lifting gas density (kg/m}^3\text{)}$$
$$m_B : \text{Mass of the balloon system (kg)}$$
$$m_p : \text{Payload mass (kg)}$$
$$C_D : \text{Drag coefficient (dimensionless)}$$
$$g : \text{Gravitational acceleration } (\approx 9.81\,\text{m/s}^2)$$

In many cases, the balloon continues to ascend beyond 30 km at an approximately constant rate of around 5 m/s (approximately 1000 ft/min), even though many parameters such as atmospheric density, balloon volume, drag, and temperature are continuously changing.

3.3.2 Balloon–UAV Transition Concept

The proposed system operates as a two-stage aerial platform consisting of a high-altitude balloon and a fixed-wing unmanned aerial vehicle (UAV). The balloon serves as a lifting mechanism to transport the UAV to a desired altitude, after which the UAV is released to perform a controlled gliding flight.

During ascent, the balloon experiences varying atmospheric conditions, including decreasing air density and pressure with increasing altitude. Despite these variations, the balloon maintains a quasi-steady ascent due to the balance between buoyant force and aerodynamic drag.
At the target altitude, the UAV is released from the balloon system. The release process is designed to ensure minimal disturbance to the UAV's initial orientation and velocity. This is critical for maintaining stability and preventing abrupt changes in flight dynamics.
Upon release, the UAV transitions from a supported system to an independent aerodynamic system. At this point, the aircraft immediately begins to generate lift through its wing surfaces while simultaneously experiencing drag and gravitational forces. The UAV is designed such that it naturally enters a stable glide condition without requiring complex control inputs.
The transition phase is governed by:

- Initial altitude and velocity at release
- Aircraft aerodynamic characteristics
- Stability about longitudinal, lateral, and directional axes

The UAV's design ensures that it possesses inherent aerodynamic stability, allowing it to align with the relative airflow and establish steady gliding flight shortly after deployment. This eliminates the need for active propulsion and enables efficient energy utilization through controlled descent.

3.3.3 Fixed-Wing UAV Aerodynamics and Stability

Fixed-wing UAVs are aircraft that generate lift through aerodynamic surfaces (wings) and are capable of sustained flight by converting aerodynamic forces efficiently. These UAVs are widely used for autonomous missions, surveillance, and experimental payload testing due to their high efficiency and stability.

3.3.3.1 Aerodynamics

Aerodynamics refers to the study of the motion of air and the forces generated when it interacts with the aircraft. It focuses on the generation of lift and drag forces and their role in determining the efficiency and performance of the UAV.

1. **Wing Design**
   (a) Fixed-wing UAVs typically employ wings with moderate to high aspect ratios to improve aerodynamic efficiency and reduce induced drag.
   (b) The airfoil selection plays a critical role in determining flight characteristics. Cambered airfoils are commonly used to provide:
      - Improved lift generation at low speeds
      - Better aerodynamic efficiency
      - Predictable and smooth stall behavior

(c) The wing structure is usually supported by spars and designed to maintain structural rigidity while minimizing interference drag at the wing–fuselage junction.

2. **Fuselage and Surface Blending**

   (a) The fuselage of a UAV is designed with a streamlined profile to minimize drag and ensure smooth airflow over the body.

   (b) Smooth transitions between the fuselage and control surfaces reduce excrescence drag caused by joints, gaps, and surface discontinuities.

3. **Drag Reduction Features**

   (a) Drag reduction is a critical design consideration in UAV aerodynamics. Parasite drag can be minimized by reducing surface roughness and avoiding unnecessary protrusions.

   (b) Careful shaping of leading edges and maintaining smooth surface continuity help in preserving laminar flow, thereby reducing drag and improving efficiency.

3.3.3.2 Stability

Aircraft stability refers to the ability of an aircraft to return to its equilibrium condition after a disturbance.

(a) **Longitudinal Stability (Pitch)**

   i. Longitudinal stability ensures that the aircraft maintains stable pitch behavior about its lateral axis.

   ii. This stability is primarily governed by the relative position of the center of gravity (CG) and the aerodynamic center. A properly positioned CG ensures that the aircraft naturally resists pitching disturbances.

   iii. The horizontal tailplane provides a restoring moment that helps maintain equilibrium in pitch.

(b) **Lateral Stability (Roll)**

   i. Lateral stability is associated with the aircraft's ability to resist rolling motions.

   ii. Features such as wing dihedral contribute to roll stability by generating restoring moments when the aircraft is disturbed.

   iii. Ailerons provide control authority to actively control the roll motion when required.

(c) **Directional Stability (Yaw)**

   i. Directional stability ensures that the aircraft maintains its heading and resists unwanted yawing motion.

   ii. The vertical stabilizer (fin) plays a crucial role in providing yaw damping and maintaining directional stability, especially during disturbances such as crosswinds.

3.3.4 Gliding Flight Theory

A glider is an unpowered fixed-wing aircraft that sustains flight by converting its gravitational potential energy into forward motion while continuously descending. Unlike powered aircraft, the energy required to overcome aerodynamic drag is obtained from the loss of altitude. Consequently, the performance of a glider is primarily governed by its aerodynamic efficiency.
Consider a glider descending steadily at a small glide angle γ relative to the horizontal. The forces acting on the aircraft are lift L, drag D, and weight W. Resolving the forces along and perpendicular to the flight path for steady flight:

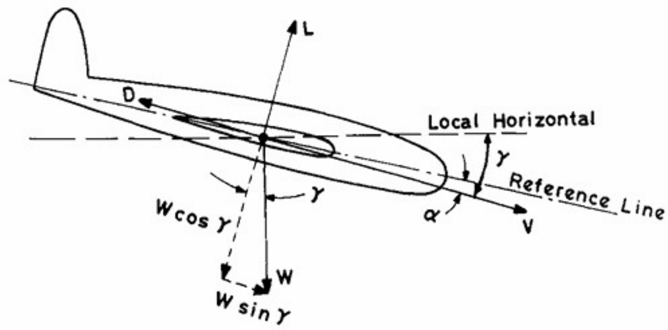

Figure 3.4: Power-off gliding flight

$$L = W\cos\gamma \tag{3.19}$$

$$D = W\sin\gamma \tag{3.20}$$

For typical gliding flight, the glide angle is small, and the above relations may be approximated as:

$$L \approx W, \quad D \approx W\gamma \tag{3.21}$$

From these relations, the glide angle is given by:

$$\tan\gamma = \frac{D}{L} \tag{3.22}$$

3.3.4.1 Aerodynamic Representation

The lift and drag forces are expressed as:

$$L = \frac{1}{2}\rho V^2 S C_L \tag{3.23}$$

$$D = \frac{1}{2}\rho V^2 S C_D \tag{3.24}$$

where ρ is the air density, V is the flight velocity, S is the wing reference area, and C_L, C_D are the lift and drag coefficients, respectively.
The drag coefficient is commonly represented as:

$$C_D = C_{D0} + kC_L^2 \tag{3.25}$$

where C_{D0} is the parasitic drag coefficient and kC_L^2 represents induced drag.

3.3.4.2 Glide Ratio and Range

The aerodynamic efficiency of a glider is measured by the lift-to-drag ratio:

$$\frac{L}{D} \tag{3.26}$$

This ratio is also equal to the glide ratio, defined as the horizontal distance traveled per unit altitude lost. For a descent from an initial height h_i to a final height h_f, the total horizontal range R is given by:

$$R = \left(\frac{L}{D}\right)(h_i - h_f) \tag{3.27}$$

Maximum range is achieved when the lift-to-drag ratio is maximized. This condition corresponds to the flattest glide trajectory.

3.3.4.3 Velocity for Best Glide

Using the lift equation with $L \approx W$, the flight velocity can be expressed as:

$$V = \sqrt{\frac{2W}{\rho S C_L}} \tag{3.28}$$

At the condition of maximum L/D, the corresponding lift coefficient is:

$$C_L = \sqrt{\frac{C_{D0}}{k}} \tag{3.29}$$

The velocity at this condition is referred to as the *best glide speed*, which provides maximum horizontal distance for a given altitude.

3.3.4.4 Sink Rate and Endurance

The rate of descent, or sink rate, is defined as the vertical component of velocity:

$$V_s = V \sin\gamma \tag{3.30}$$

For small glide angles:

$$V_s \approx \frac{V}{L/D} \tag{3.31}$$

The total flight time (endurance) is given by:

$$t = \frac{h}{V_s} \tag{3.32}$$

Minimum sink rate corresponds to maximum endurance.

3.3.4.5 Condition for Minimum Sink

The minimum sink condition occurs when the following parameter is maximized:

$$\frac{C_L^{3/2}}{C_D} \tag{3.33}$$

This leads to the condition:

$$C_L = \sqrt{\frac{3C_{D0}}{k}} \tag{3.34}$$

At this operating point, the induced drag is three times the parasitic drag. The corresponding velocity is lower than the best glide speed and is approximately:

$$V_{\text{min sink}} \approx 0.76 V_{\text{best glide}} \tag{3.35}$$

3.3.4.6 Performance Characteristics

Two key performance conditions govern gliding flight:

- Maximum Range: Achieved at maximum L/D, corresponding to the flattest glide path.
- Maximum Endurance: Achieved at minimum sink rate, corresponding to longer time aloft.

Maximum range is largely independent of weight, whereas endurance is influenced by the aircraft weight and aerodynamic characteristics.

3.3.4.7 Effect of External Factors

Environmental conditions significantly influence gliding performance. A headwind reduces the ground range, while a tailwind increases it. Crosswinds introduce lateral drift, affecting navigation accuracy. Variations in air density with altitude also affect aerodynamic forces and flight velocity.

3.3.4.8 Design Implications

Efficient gliding flight requires a high lift-to-drag ratio, low parasitic drag, high aspect ratio wings, and smooth aerodynamic surfaces. These factors collectively enhance range, reduce sink rate, and improve overall flight performance.

3.4 Preliminary Aerodynamic Design (XFLR5)

The preliminary aerodynamic design of the UAV was carried out using XFLR5, which served as an initial design and analysis tool prior to fabrication. The primary objective of using XFLR5 was to estimate the aerodynamic characteristics of the UAV, including lift generation, drag behavior, and overall stability, under low-speed flight conditions typical of a glider. An appropriate airfoil was selected based on its performance in low Reynolds number regimes, ensuring sufficient lift generation and stable glide characteristics.

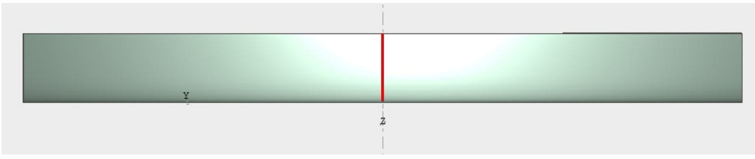

Figure 3.5: Selected wing geometry

The wing geometry was designed with a wingspan of 1.8 m and an approximate wing area of 0.27 m², resulting in a high aspect ratio configuration suitable for gliding flight. A rectangular wing planform was selected due to its simplicity in design, ease of fabrication, and predictable aerodynamic behavior. The expected flight speed of the UAV was around 11 m/s, and aerodynamic analysis was conducted across a range of angles of attack from -5° to 16° to evaluate performance over typical operating conditions. Both two-dimensional airfoil analysis and three-dimensional full aircraft analysis were performed in XFLR5. The complete configuration, including wing and tail, was modeled to capture realistic aerodynamic interactions. The center of gravity (CG) location was estimated during the design phase and positioned near 25 percent of the mean aerodynamic chord (MAC) to ensure static stability. The analysis indicated that the UAV configuration was statically stable, making it suitable for gliding and controlled descent after deployment. It is important to note that XFLR5 was used strictly as a preliminary design tool, and the results obtained from this stage were later validated through physical testing and flight experiments.

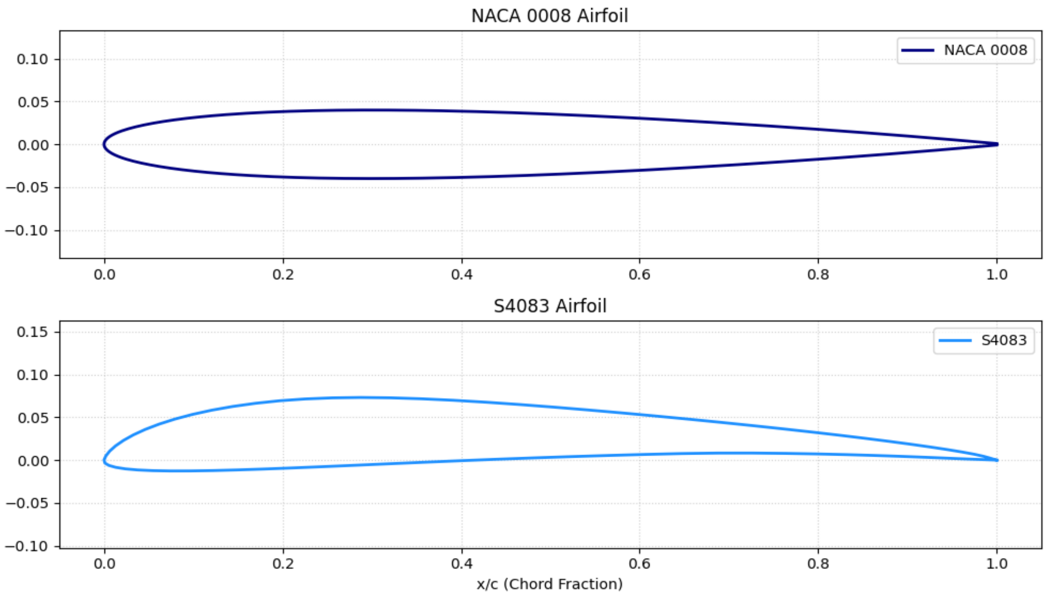

Figure 3.6: Airfoils used

The UAV developed in this project is a lightweight fixed-wing glider designed for balloon assisted deployment and autonomous descent. The primary objective of the design was to achieve stable gliding performance while maintaining a lightweight structure capable of carrying onboard avionics and power systems. The total weight of the final UAV prototype was approximately 700 grams, including the structural components, battery, and avionics system.

3.4.1 Final UAV/Glider Parameters

Parameter	**Value**
Wingspan	1.8 m
Wing Area	0.27 m^2
Aspect Ratio	12
Wing Type	Rectangular
Airfoil	S4083
Tail Type	Conventional
Fuselage	Carbon fiber rod
Weight	700 g
Speed	11 m/s

Table 3.1: UAV/Glider Parameters

3.5 Analytical Estimation of Glide Performance

The analytical glide performance of the fixed-wing UAV was estimated using classical unpowered glide theory. The UAV parameters and assumptions are summarized below.

3.5.1 Aircraft and Aerodynamic Parameters

- Wingspan: $b = 1.8$ m
- Wing area: $S = 0.270$ m^2
- Aspect Ratio: $AR = 12$
- Mass: $m = 0.700$ kg
- Weight: $W = mg = 0.700 \times 9.81 \approx 6.86$ N
- Oswald Efficiency Factor: $e = 0.7$
- Zero-lift Drag Coefficient: $C_0 = 0.045$
- Air density at test site: $\rho = 1.07$ kg/m^3

An Oswald efficiency factor of $e = 0.7$ and zero-lift drag coefficient of $C_{D0} = 0.045$ were assumed based on typical values for small fixed-wing UAVs, accounting for non-ideal aerodynamic effects and practical parasitic drag losses.

3.5.2 Induced Drag Factor

The induced drag factor k is calculated using:

$$k = \frac{1}{\pi ARe} \tag{3.36}$$

Substituting the values:

$$k = \frac{1}{\pi \times 12 \times 0.7} \approx 0.037 \tag{3.37}$$

3.5.3 Maximum Glide Efficiency

Maximum lift-to-drag ratio is given by:

$$\left(\frac{L}{D}\right)_{\max} = E_{\max} = \frac{1}{2\sqrt{kC_0}} \tag{3.38}$$

$$E_{\max} = \frac{1}{2\sqrt{0.037 \cdot 0.045}} \approx 12.253 \tag{3.39}$$

3.5.4 Maximum Theoretical Glide Range

Assuming an effective altitude loss $\Delta h = 43$ m after stabilisation:

$$R_{\max} = \Delta h \cdot E_{\max} = 43 \times 12.253 \approx 526.87 \text{ m} \tag{3.40}$$

3.5.5 Minimum Glide Angle

The minimum glide path angle $\gamma_{\min}$ is:

$$\gamma_{\min} = \arctan\left(\frac{1}{E_{\max}}\right) \tag{3.41}$$

$$\gamma_{\min} = \arctan\left(\frac{1}{12.253}\right) \approx 4.676^\circ \tag{3.42}$$

3.5.6 Lift Coefficient at Minimum Sink

Lift coefficient at minimum sink:

$$C_L^* = \sqrt{\frac{C_0}{k}} = \sqrt{\frac{0.045}{0.037}} \approx 1.103 \tag{3.43}$$

3.5.7 Drag Coefficient at Minimum Sink

$$C_{D,ms} = C_0 + k(C_L^*)^2 = 0.045 + 0.037 \times (1.103)^2 \approx 0.089 \tag{3.44}$$

3.5.8 Endurance Parameter

$$\left(\frac{C_L^{3/2}}{C_D}\right)_{\max} = \frac{(C_L^*)^{3/2}}{C_{D,ms}} = \frac{(1.103)^{3/2}}{0.089} \approx 13.01 \tag{3.45}$$

3.5.8.1 Velocity for Best Endurance

Flight velocity for minimum sink:

$$V = \sqrt{\frac{2W}{\rho S}}\left(\frac{k}{3C_0}\right)^{1/4} \tag{3.46}$$

$$V = \sqrt{\frac{2 \times 6.86}{1.07 \times 0.270}}\left(\frac{0.037}{3 \times 0.045}\right)^{1/4} \approx 5.072 \text{ m/s} \tag{3.47}$$

3.5.9 Maximum Endurance

Maximum glide endurance:

$$t_{\max} = \sqrt{\frac{\rho S}{2W}}\left(\frac{27}{k^3 C_0}\right)^{1/4} \frac{h}{4} \tag{3.48}$$

$$t_{\max} = \sqrt{\frac{1.07 \times 0.270}{2 \times 6.86}}\left(\frac{27}{0.037^3 \cdot 0.045}\right)^{1/4} \frac{43}{4} \approx 80.27 \text{ s} \tag{3.49}$$

3.5.10 Minimum Sink Rate

Minimum vertical speed:

$$V_{s,\min} = \sqrt{\frac{2W}{\rho S}} \left(\frac{kC_0}{27} \right)^{1/4} \tag{3.50}$$

$$V_{s,\min} = \sqrt{\frac{2 \times 7.4}{1.07 \times 0.270}} \left(\frac{0.037 \cdot 0.045}{27} \right)^{1/4} \approx 0.610 \text{ m/s} \tag{3.51}$$

3.6 UAV Design and Fabrication

3.6.1 Structural Design

The UAV consists of three primary components: wing, fuselage, and tail. The wing was constructed using foam as the primary material, shaped using a GRBL-based hot wire cutting process to achieve the desired airfoil profile. Internal spars were incorporated to provide structural rigidity while maintaining low weight. The fuselage underwent multiple design iterations. Initial prototypes used a foam-based fuselage; however, due to structural limitations and weight considerations, the final design utilized a carbon fiber rod as the main fuselage member. This configuration significantly reduced weight while providing sufficient structural strength. The carbon rod connects the nose section, wing, and tail assembly in a streamlined manner.

Figure 3.7: Wing

A 3D-printed nose section was designed using SolidWorks and fabricated using PLA material. This nose houses the battery at the front, which also helps in maintaining proper center of gravity. The flight controller was mounted above the wing near the CG location to ensure stable flight characteristics.

Figure 3.8: Nose

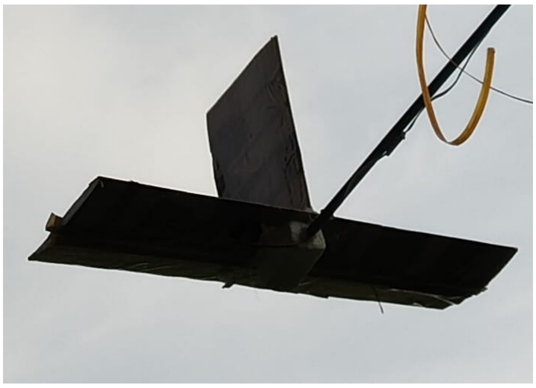

Figure 3.9: Tail

The UAV employs a conventional tail configuration, consisting of horizontal and vertical stabilizers. The tail size was increased in the final design to improve stability and control effectiveness during glide.

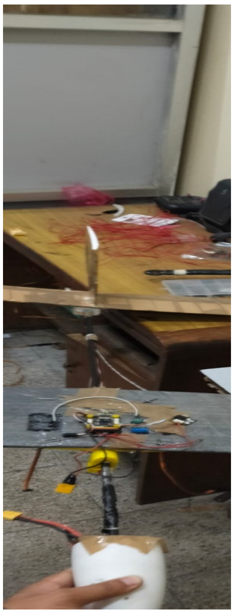

Figure 3.10: Fuselage

3.6.2 Manufacturing Process

The design and fabrication process involved a combination of digital modeling and physical manufacturing techniques. The nose section and mounting components were designed using SolidWorks and fabricated through 3D printing using PLA material. The wings were manufactured using a hot wire cutting technique, which ensured accurate airfoil shaping and smooth surface finish.

Figure 3.11: PLA

Foam was selected as the primary material due to its lightweight properties and ease of fabrication. Other structural components were assembled using adhesives and mechanical fittings, ensuring proper alignment and structural integrity of the overall system.

3.6.3 Avionics and Integration

The UAV is equipped with a SpeedyBee F405 Wing flight controller, which serves as the central onboard unit for flight stabilization and control. The controller was selected due to its lightweight and suitability for fixed-wing UAV applications. The system integrates key sensors, including an inertial measurement unit (IMU), GPS module, and barometer, enabling real-time estimation of attitude, position, and altitude during flight. The control system was configured to operate in a stabilized flight mode, in which the flight controller automatically compensates for disturbances by adjusting control surface deflections based on sensor feedback. This feature is particularly important for this application, as the UAV experiences transient disturbances immediately after release. A PID-based control strategy was implemented to regulate attitude dynamics, reducing oscillations in pitch and roll and enabling a smooth transition into steady gliding flight. The avionics components were securely integrated within the airframe with proper attention to wiring, vibration resistance, and reliable power distribution, ensuring consistent performance during flight testing.

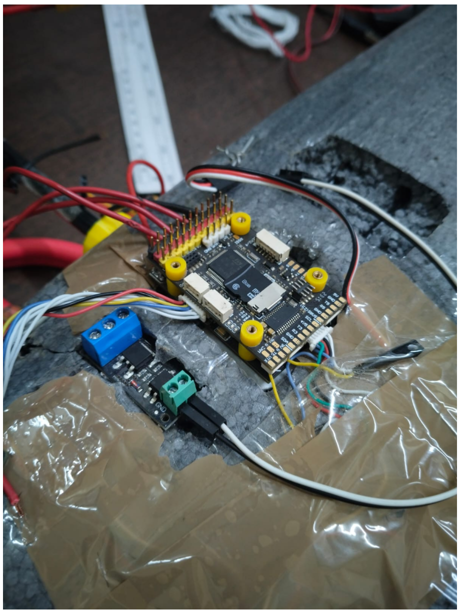

Figure 3.12: SpeedyBee F405

Figure 3.13: Servo

3.6.4 Design Iterations and Prototype Development

During the course of the project, four different UAV prototypes were developed and tested to progressively improve aerodynamic performance, structural efficiency, and system integration.

1. **Prototype 1:**
   The initial design had a smaller wing and low aspect ratio, resulting in poor glide performance. Additionally, it lacked sufficient space to accommodate onboard electronics and battery systems.

Figure 3.14: Prototype 1

2. **Prototype 2:**
   The second design featured an increased aspect ratio, improving lift characteristics. However, it was more similar to an RC aircraft configuration, making it less suitable for pure gliding applications and resulting in inefficient descent behavior.

Figure 3.15: Prototype 2

3. **Prototype 3:**
   The third prototype incorporated further aerodynamic improvements but had a higher overall weight (approximately 1 kg), which affected glide efficiency despite improved lift generation.

Figure 3.16: Prototype 3

4. **Prototype 4 (Final Design)**
   The final UAV achieved a balanced and optimized design, featuring a larger wingspan, reduced weight (700g), improved CG placement, and a cleaner aerodynamic configuration. The tail size was increased for better control, and the use of a carbon fiber fuselage significantly enhanced structural efficiency. This configuration demonstrated the best glide performance and stability among all prototypes.

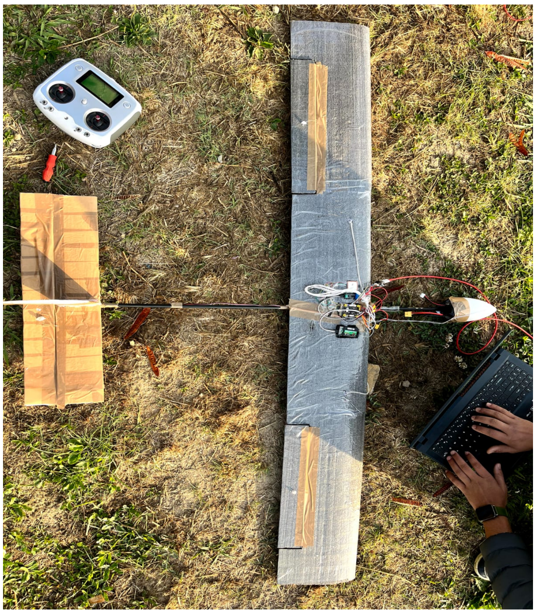

Figure 3.17: Prototype 4

3.7 Deployment System Design

To deploy the Fixed-Wing UAV from the balloon we have designed a release mechanisms:

3.7.1 Nichrome Burn Wire

A nichrome burn wire mechanism is a simple, lightweight, and reliable release system commonly used in high-altitude balloons, UAV deployment, and aerospace payload release mechanisms. It works by heating a nichrome wire to the point where it melts or cuts through a cable .The release mechanism, shown in Figure 3.2, utilizes a two saddle design with compression springs to apply a spring stroke and force to the nichrome wire to thermally cut through the Nylon cable when heated. To activate the nichrome wire a constant current of 1.60 ± 0.05 amps is applied to ensure a successful and reliable cut. The tight tolerance constant current source is necessary in order to reliably: 1.) thermally cut the cable and 2.) prevent overheating failure of the nichrome wire to allow the mechanism to be reusable for many actuations without replacing the nichrome filament. [9]

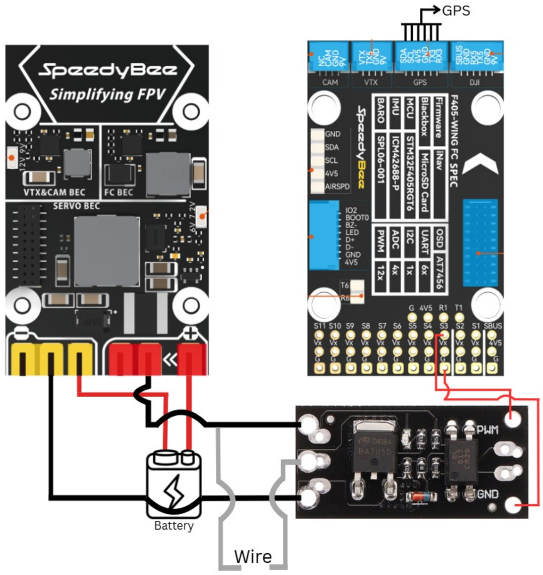

Figure 3.18: Electronic release system showing SpeedyBee F405 flight controller, MOSFET, burn-wire, and battery integration.

Working

(a) **Nichrome wire setup:**
The release mechanism, utilizes a nichrome wire. When a constant current is applied to the nichrome wire, it will thermally cut through a tie down cable allowing it to release the UAV.

(b) **Tether or line:**
A high-strength, low-melting-point material (like fishing line or nylon) is wrapped around or passed under the nichrome wire which is cut down.

(c) **Trigger:**
A microcontroller or timer or upon reaching certain altitude activates the circuit .A battery supplies current to the Nichrome wire.

(d) **Heating:**
Nichrome wire has high resistance, so when current passes through it, it heats up quickly to 300–1200°C.This heat burns through or melts the tether and the UAV is released.

3.8 Stability and Control Design

The stability and control characteristics of the glider UAV were designed to ensure predictable aerodynamic behavior and reliable recovery following aerial deployment. Since the aircraft is released from altitude rather than launched conventionally, achieving inherent static stability was a primary design requirement.

A conventional tail configuration was selected due to its simplicity and well-established aerodynamic performance. The center of gravity (CG) was positioned near 25 percent of the mean aerodynamic chord (MAC), ensuring positive longitudinal static stability. This configuration provides a restoring pitching moment, allowing the aircraft to naturally return to its equilibrium condition after disturbances.

To further enhance stability, the tail surfaces were sized slightly larger than the minimum requirement. This increased tail volume improves both longitudinal and directional stability, which is particularly important during the initial transient phase immediately after release.

Control was achieved using two ailerons for roll control and one elevator for pitch control, providing sufficient authority to maintain stable gliding behavior within the intended flight envelope.

The overall configuration was designed to provide stable, non-oscillatory gliding behavior with adequate control authority, ensuring a smooth and controlled descent throughout the flight envelope.

3.8.1 Electrical System

The deployment system was powered by a dedicated onboard battery supply, which provided the electrical energy required to heat the nichrome wire during release. The electrical circuit was designed to ensure safe and controlled activation of the thermal cutting mechanism.

The main components of the electrical system included:

- Battery power source
- Nichrome wire heating element
- MOSFET-based switching circuit
- Trigger/control input (manual or controller-based)

A MOSFET switch was used as the primary control element to handle the high current required by the nichrome wire. Since the nichrome wire draws approximately 1.6 A, direct switching through low-power control electronics is not feasible. The MOSFET functions as an electronically controlled high-current switch, enabling safe and efficient current flow through the heating element.

When a trigger signal is applied, the MOSFET activates and allows current to pass through the nichrome wire. The resulting resistive heating causes the wire to reach a high temperature, cutting the nylon tether and initiating release.

In the initial testing phase, the system was activated manually from the ground to ensure safe verification of the release mechanism. This allowed controlled observation of the cutting process and reduced risk during early validation.

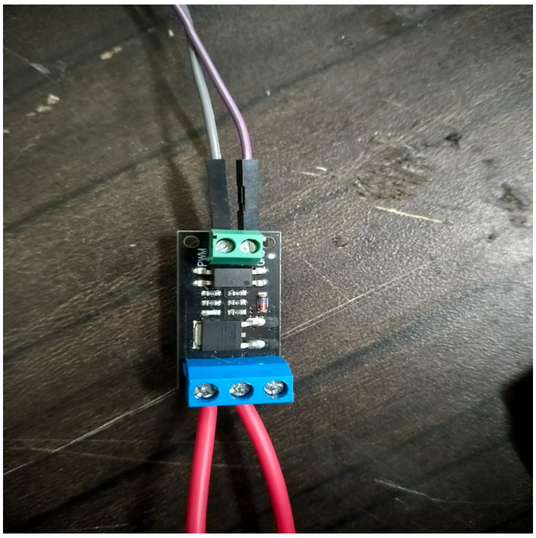

Figure 3.19: MOSFET

The electrical system was designed with the following objectives:

- Reliable current delivery to the nichrome wire
- Safe isolation between control electronics and heating load
- Simple and compact integration with the carrier platform
- Repeatable and consistent activation during deployment tests

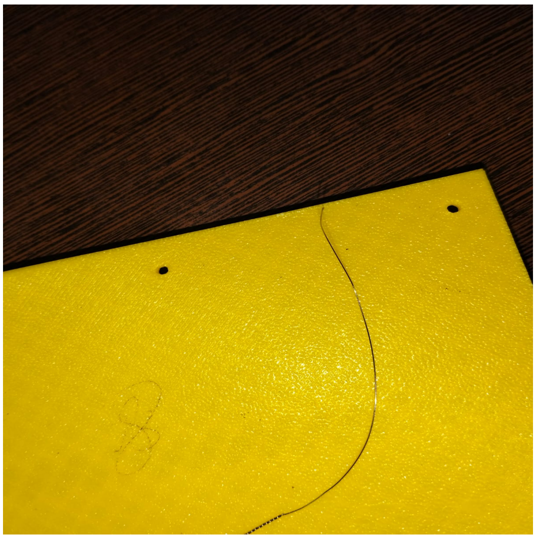

Figure 3.20: Nichrome wire

3.8.2 System Integration

The deployment mechanism was integrated such that the glider UAV was suspended beneath the aerial carrier using a nylon tether system. The tether passed through the nichrome wire release assembly, which served as the controlled separation point between the carrier and the glider.

The mounting configuration ensured:

- Proper center of gravity alignment during carriage
- Adequate clearance from the carrier structure
- Stable suspended orientation prior to release
- Minimal interference with the glider's aerodynamic surfaces

The configuration allowed clean separation once the tether was cut, enabling the glider to transition smoothly into free flight without entanglement or collision with the carrier.

Initial deployment tests were conducted under controlled low-risk conditions to verify:

- Mechanical integrity of the release assembly
- Structural security of the tether connection
- Response of the electrical triggering system
- Clean separation behavior after release

Following validation, the system was tested using a DJI Phantom 4 as the carrier platform. This provided higher release altitude, improved control over deployment conditions, and increased repeatability of tests, resulting in more realistic evaluation of the glider's post-release stability and performance.

3.9 Selection of Lifting Balloon and Buoyancy-Based Sizing Analysis for Balloon-Deployed UAV Deployment

The selection of the lifting balloon was a critical part of the balloon-deployed UAV system because the overall success of the deployment depended directly on the balloon's ability to safely retain hydrogen gas, generate adequate buoyant lift, and provide stable suspension of the glider payload prior to release. During the initial phase of the project, a custom-fabricated polyethylene balloon was developed with the intention of creating a lightweight and low-cost lifting envelope that could be tailored to the project requirements. The fabricated balloon was expected to serve as the primary lifting body for the glider deployment system. However, during preliminary inflation trials, the polyethylene balloon repeatedly exhibited gas leakage at the seam and joint regions, resulting in an inability to maintain internal pressure for a sufficient duration. Since hydrogen retention is one of the most important functional requirements of any buoyant lifting system, this repeated leakage significantly reduced the reliability of the fabricated balloon and made it unsuitable for practical deployment. Due to this limitation, the fabricated polyethylene balloon was rejected, and the project shifted to the use of a commercial latex balloon, which provided better sealing, improved structural integrity during inflation, more consistent geometry, and greater practical reliability for hydrogen-based lifting applications.

After the rejection of the fabricated polyethylene envelope, a 32-inch latex balloon was selected for the final experimental configuration of the balloon-deployed UAV system. The use of a latex balloon was preferred because it was readily available, easier to handle during filling, capable of maintaining hydrogen gas more effectively than the fabricated envelope, and more suitable for repeatable experimental testing. In order to determine whether the selected latex balloon could provide sufficient lift for the intended payload, a first-order buoyancy-based sizing analysis was performed. The nominal diameter of the selected balloon when fully inflated was taken as 32 inches, which is equivalent to:

$$D = 32 \times 0.0254 = 0.8128\,\text{m} \tag{3.52}$$

Assuming the balloon to be approximately spherical for engineering estimation, the radius of the balloon becomes:

$$r = \frac{D}{2} = \frac{0.8128}{2} = 0.4064\,\text{m} \tag{3.53}$$

The internal volume of the balloon was then estimated using the standard volume relation for a sphere:

$$V = \frac{4}{3}\pi r^3 \tag{3.54}$$

Substituting the radius value:

$$V = \frac{4}{3}\pi(0.4064)^3 \approx 0.281\,\text{m}^3 \tag{3.55}$$

Thus, the selected 32-inch latex balloon was estimated to have an internal volume of approximately:

$$V \approx 0.281\,\text{m}^3 = 281\,\text{L} \tag{3.56}$$

This indicates that approximately $0.281\,\text{m}^3$, or 281 L, of hydrogen gas is required to fully inflate one 32-inch latex balloon under near-atmospheric conditions. This value is highly important for practical field preparation because it directly determines the gas generation or storage requirement before deployment. For project-level planning, this means that each individual balloon requires roughly 280 L of hydrogen gas, with a small additional margin typically recommended to compensate for handling losses, non-ideal inflation conditions, and the slightly lower lifting efficiency of non-pure hydrogen.

Figure 3.21: Latex balloon

To evaluate the lifting performance of the balloon, the buoyant force was estimated using Archimedes' principle, which states that the net lifting capability of a gas balloon depends on the difference between the density of ambient air and the density of the lifting gas. Since the experimental work was conducted in the Lalitpur/Kathmandu region, where the elevation is significantly higher than sea level, the ambient air density is lower than standard sea-level conditions. For the present first-order estimation, the air density in the Kathmandu valley was taken as approximately:

$$\rho_{air} \approx 1.07\,\text{kg/m}^3 \tag{3.57}$$

The density of hydrogen under near-atmospheric conditions was taken as:

$$\rho_{H_2} \approx 0.084\,\text{kg/m}^3 \tag{3.58}$$

The gross buoyant lift generated by one balloon is therefore given by:

$$L_{\text{gross}} = (\rho_{air} - \rho_{H_2})V \tag{3.59}$$

Substituting the above values:

$$L_{\text{gross}} = (1.07 - 0.084)(0.281) \tag{3.60}$$

$$L_{\text{gross}} \approx 0.277\,\text{kg} \tag{3.61}$$

Therefore, the theoretical gross lifting capacity of a single 32-inch hydrogen-filled latex balloon under Kathmandu/Lalitpur atmospheric conditions is approximately:

$$L_{\text{gross}} \approx 277\,\text{g} \tag{3.62}$$

This value represents the ideal buoyant lift before accounting for the mass of the balloon itself, the neck tie, suspension string, tape, tether, release loop, and any other attachment hardware. In practical operation, these additional components reduce the actual usable lift available for supporting the glider. Considering that a large latex balloon typically has a self-weight in the range of 35–50 g, and the suspension accessories may add an additional 10–20 g, the effective usable lift per balloon is reduced to approximately:

$$L_{\text{usable}} \approx 220 \text{ to } 235\,\text{g} \tag{3.63}$$

For conservative engineering calculations and safer design margins, the usable lift per balloon was approximated as:

$$L_{\text{usable}} \approx 230\,\text{g} \tag{3.64}$$

This practical value was then used to estimate the number of balloons required to lift the final glider payload. The all-up mass of the glider selected for the deployment system was approximately 750 g. Considering that hydrogen is not perfectly pure and that the 32-inch balloons will not be fully inflated for safety, a slightly higher margin of lift is required. Therefore, instead of five balloons, a six-balloon configuration is recommended to ensure reliable deployment.

For a six-balloon configuration, the total hydrogen gas requirement becomes:

$$V_6 = 6 \times 281 = 1686\,\text{L} \tag{3.65}$$

$$V_6 = 1.686\,\text{m}^3 \tag{3.66}$$

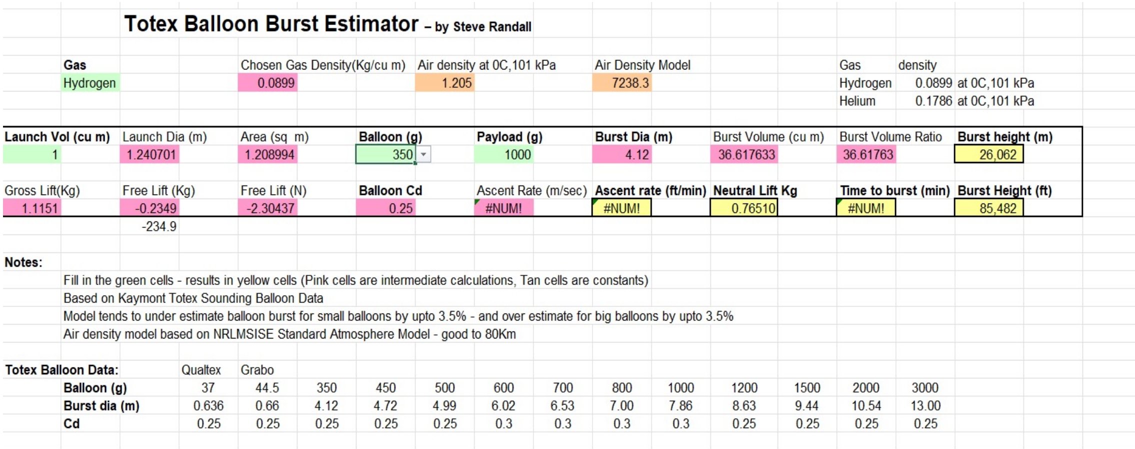

Totex Balloon Burst Estimator – by Steve Randall

Gas	Chosen Gas Density(Kg/cu m)	Air density at 0C,101 kPa	Air Density Model
Hydrogen	0.0899	1.205	7238.3

Gas	density	
Hydrogen	0.0899	at 0C,101 kPa
Helium	0.1786	at 0C,101 kPa

Launch Vol (cu m)	Launch Dia (m)	Area (sq m)	Balloon (g)	Payload (g)	Burst Dia (m)	Burst Volume (cu m)	Burst Volume Ratio	Burst height (m)
1	1.240701	1.208994	350	1000	4.12	36.617633	36.61763	26,062
Gross Lift(Kg)	**Free Lift (Kg)**	**Free Lift (N)**	**Balloon Cd**	**Ascent Rate (m/sec)**	**Ascent rate (ft/min)**	**Neutral Lift Kg**	**Time to burst (min)**	**Burst Height (ft)**
1.1151	-0.2349	-2.30437	0.25	#NUM!	#NUM!	0.76510	#NUM!	85,482
	-234.9							

Notes:

Fill in the green cells - results in yellow cells (Pink cells are intermediate calculations, Tan cells are constants)
Based on Kaymont Totex Sounding Balloon Data
Model tends to under estimate balloon burst for small balloons by upto 3.5% - and over estimate for big balloons by upto 3.5%
Air density model based on NRLMSISE Standard Atmosphere Model - good to 80Km

Totex Balloon Data:	Qualtex	Grabo											
Balloon (g)	37	44.5	350	450	500	600	700	800	1000	1200	1500	2000	3000
Burst dia (m)	0.636	0.66	4.12	4.72	4.99	6.02	6.53	7.00	7.86	8.63	9.44	10.54	13.00
Cd	0.25	0.25	0.25	0.25	0.25	0.3	0.3	0.3	0.3	0.25	0.25	0.25	0.25

Figure 3.22: Totex balloon brust estimator

From an engineering and safety perspective, this configuration provides adequate reserve lift to support not only the glider mass but also the balloon self-weight, suspension line mass, release mechanism, minor operational inefficiencies, and the slightly reduced lift due to non-pure hydrogen. Furthermore, the use of multiple balloons can improve load sharing and reduce the likelihood of failure due to a single balloon under performing.

Figure 3.23: Latex balloon

From the overall design perspective, the selected balloon system was therefore governed by several critical requirements: sufficient buoyant lift to support the glider mass, reliable hydrogen retention during pre-launch handling, low self-weight to maximize usable lift, mechanical robustness during inflation and suspension, and repeatability for academic testing. The fabricated polyethylene balloon failed primarily in the requirement of gas retention, which is fundamental to any lighter-than-air lifting system, whereas the latex balloon successfully met the practical requirements of sealing, handling, availability, and repeatability. Based on the buoyancy analysis, it was concluded that a single 32-inch latex balloon is insufficient for lifting a 750 g glider, and that the system requires a minimum of four balloons, while a six-balloon configuration is recommended for safe and reliable experimental deployment.

Figure 3.24: Sealing machine

This configuration provides a realistic balance between gas requirement, lift capacity, and operational reliability, making it the most suitable choice for the balloon-deployed UAV proof-of-concept system developed in this project.

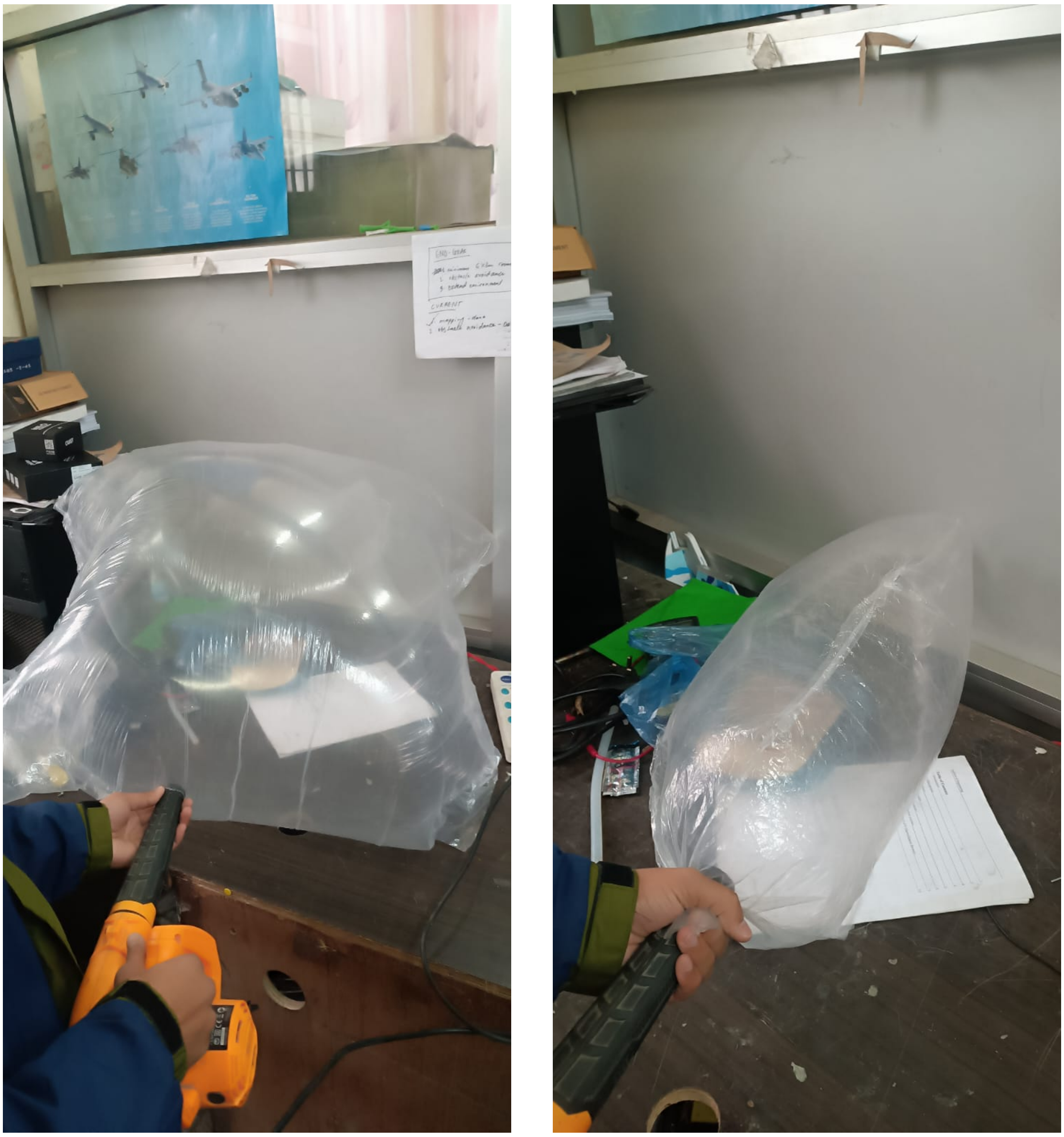

Figure 3.25: Balloon fabrication.

3.9.1 Deployment Testing

A series of deployment tests were conducted to validate the functionality, repeatability, and safety of the release mechanism before and during aerial trials. The purpose of these tests was to confirm that the nichrome wire system could consistently release the UAV under practical operating conditions.

3.9.2 Initial Testing

The first stage of deployment testing was performed using the assembled UAV system in a controlled ground-based configuration. These tests focused on verifying:

(a) Correct electrical activation of the nichrome wire

(b) Heating response time
(c) Successful cutting of the nylon tether
(d) Structural integrity of the attachment arrangement
(e) Clean release without snagging or mechanical interference

This phase allowed the release mechanism to be evaluated safely before introducing the additional complexity of aerial deployment.

3.9.3 Improved Aerial Testing Using DJI Phantom 4

After successful initial validation, the deployment system was integrated with a DJI Phantom 4 for aerial release trials. The drone served as a controlled carrier platform, enabling the glider to be lifted to a higher altitude and released under more representative flight conditions.

Figure 3.26: DJI Phantom 4

The use of the DJI Phantom 4 improved the testing process for the following reasons:

(a) It allowed higher altitude deployment, resulting in longer glide evaluation windows
(b) It provided controlled and repeatable release conditions
(c) It reduced uncertainty in launch timing and position
(d) It allowed better observation of glider behavior immediately after release

These aerial deployment tests were essential for assessing the transition from suspended carriage to free gliding flight. The tests confirmed that the nichrome wire mechanism could release the glider reliably and that the aircraft could separate successfully from the carrier platform.

Figure 3.27: DJI Phantom 4 carrying UAV

3.9.4 Ground-Based Component and System Testing

After the development of the release mechanism, balloon cluster, and UAV airframe, all subsystems were validated through a structured ground testing programme. The UAV was secured to the release mechanism via a nylon tether, and the release mechanism was actuated to verify smooth and consistent separation.

Where full separation was not initially achieved, the mechanism was refined and re-tested until reliable performance was obtained. The balloon envelopes were subjected to leak tests to identify and repair any gas permeation prior to inflation.

Following fabrication, manual tests were conducted to evaluate the structural integrity and handling characteristics of the system in a real environment. Upon confirming a fully functional release mechanism and stable balloon performance, the integrated system was prepared for full-altitude deployment testing.

Figure 3.28: Pre-flight inspection

3.9.5 Ground Testing and Electronics Validation

Ground testing was conducted at Pulchowk Ground, Lalitpur, prior to aerial flight trials to verify that the glider airframe, onboard electronics, and control system were operating correctly under controlled conditions.

The airframe was inspected for structural integrity, including wing and tail alignment, control surface range of motion, and correct centre of gravity (CG) placement. Onboard wiring and electrical connections were checked for secure joints, correct polarity, and continuity.

The avionics system, centered on a SpeedyBee flight controller, was powered and verified for proper initialization and stable operation. Pre-flight checks confirmed correct sensor initialization and appropriate response of the control surfaces to input commands.

Special attention was given to the nichrome wire release mechanism, which was tested both as a standalone unit and in its integrated configuration. Continuity of the wire, heating response, release timing, and repeatability were evaluated and confirmed. The system was activated manually during the ground testing phase to ensure safe and controlled operation.

The ground testing phase confirmed that the airframe, avionics, control surfaces, and release system were functioning as intended, providing confidence for aerial deployment and glide-performance evaluation.

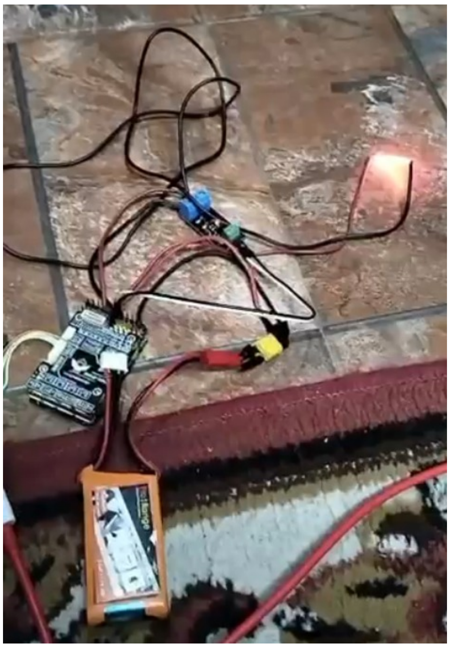

Figure 3.29: Nichrome wire heating during controlled actuation in the bench test setup.

3.10 Mission Profile

Phase No	Phase	Description
1	Ground Preparation	The UAV was mounted to the balloon cluster via the nichrome burn-wire release mechanism; battery was fully charged; and waypoints were programmed into the autopilot.
2	Balloon Launch	The balloon cluster began its ascent with the UAV secured underneath.
3	Altitude Monitoring	The onboard flight controller monitored altitude continuously using GPS and barometric sensor data.
4	Autonomous Release	Upon reaching the target altitude (20–60 m AGL), the servo-pin was activated, triggering the nichrome burn-wire and releasing the UAV.
5	Flight Activation	The UAV stabilised and transitioned to autopilot, initiating autonomous flight.
6	Loiter	The UAV entered a loiter pattern with gradual altitude descent.
7	Landing	The UAV navigated to and landed at a pre-programmed waypoint location.
8	Mission End	The UAV either returned to base (RTL) or landed autonomously at the target site.

Table 3.2: Mission Table

CHAPTER FOUR:
RESULT AND DISCUSSION

4.1 Predicted Aerodynamic Performance (XFLR5)

The aerodynamic characteristics obtained from XFLR5 provide a baseline for evaluating the UAV's expected flight performance under low Reynolds number conditions.

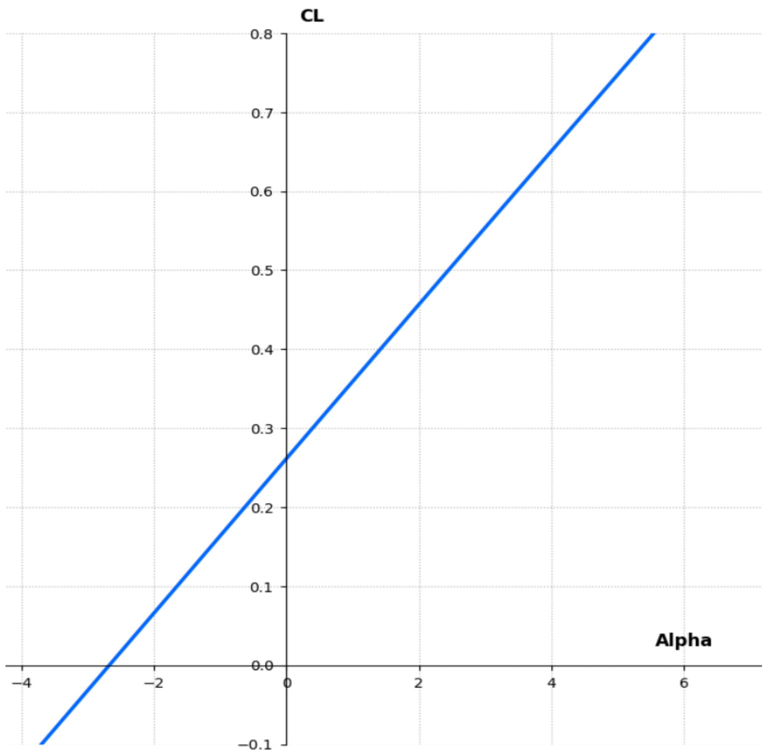

Figure 4.1: CL VS ALPHA

The variation of lift coefficient with angle of attack (Figure 7.1) shows a nearly linear trend within the operational range, indicating predictable lift generation and absence of premature stall. This behavior is essential for maintaining a stable glide during descent.

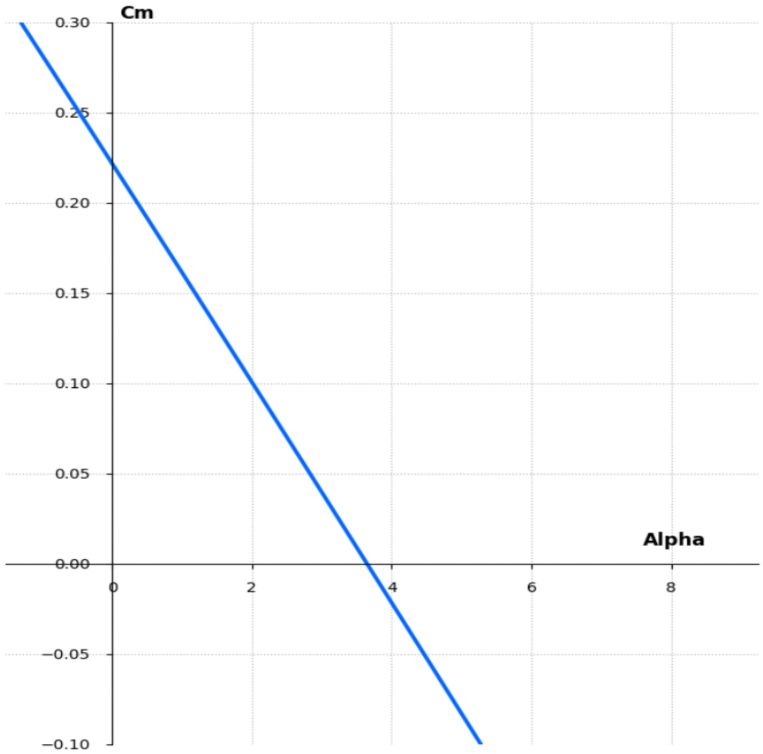

Figure 4.2: CM VS ALPHA

The pitching moment curve (Figure 7.2) exhibits a negative slope with respect to angle of attack, confirming positive static longitudinal stability. This ensures that the UAV has a natural tendency to return to equilibrium after disturbances, which is critical for autonomous gliding.

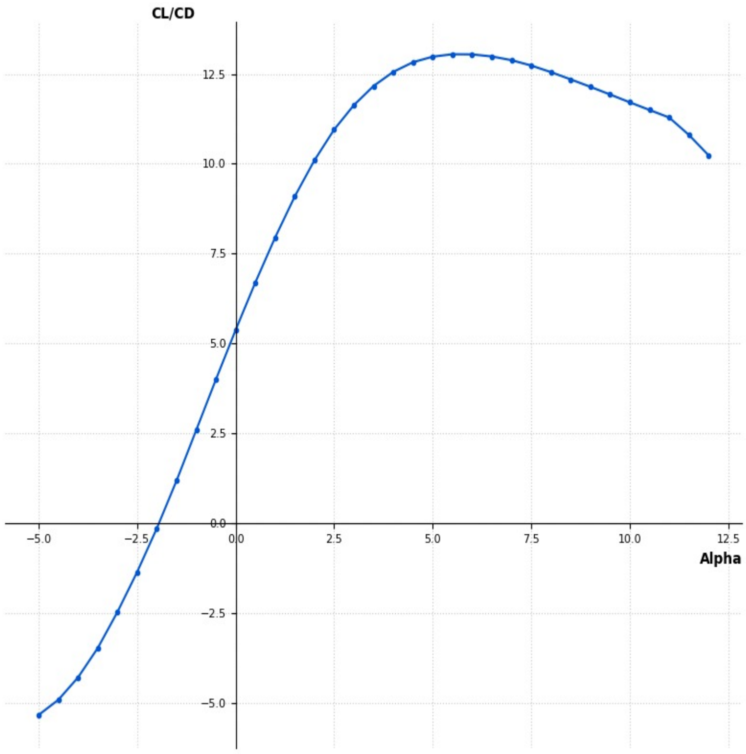

Figure 4.3: CL/CD VS ALPHA

The lift-to-drag ratio curve (Figure 7.3) indicates the aerodynamic efficiency of the UAV. The peak value corresponds to the optimal glide condition, where maximum horizontal distance can be achieved for a given altitude loss. The relatively moderate peak suggests that the UAV is optimized for stable descent rather than maximum endurance, which aligns with the mission objective.

The drag characteristics, as observed indirectly through aerodynamic efficiency trends, indicate the presence of expected parasitic and induced drag components. These effects limit glide range but contribute to controlled descent behavior.

Overall, the XFLR5 results indicate that the UAV configuration is aerodynamically stable, capable of generating sufficient lift, and suitable for controlled gliding flight, forming a reliable basis for experimental validation.

4.2 Experimental Flight Results

The flight performance of the UAV was evaluated through real-world drop tests conducted after system integration. Flight data was extracted from onboard log files.

4.2.1 Post deployment stability

4.2.1.1 Pitch vs Time

The plot illustrates the variation of pitch angle (ATTITUDE.pitch) over time. Initially, the pitch remains relatively constant at around 0.22 rad. A sudden increase in pitch is observed, reaching about 0.05 rad, indicating a significant transient event such as release or external disturbance. Following this, the pitch gradually decreases and stabilizes around 0.12 rad with minor fluctuations.

This response indicates a transient disturbance followed by gradual stabilization of the glider's longitudinal attitude.

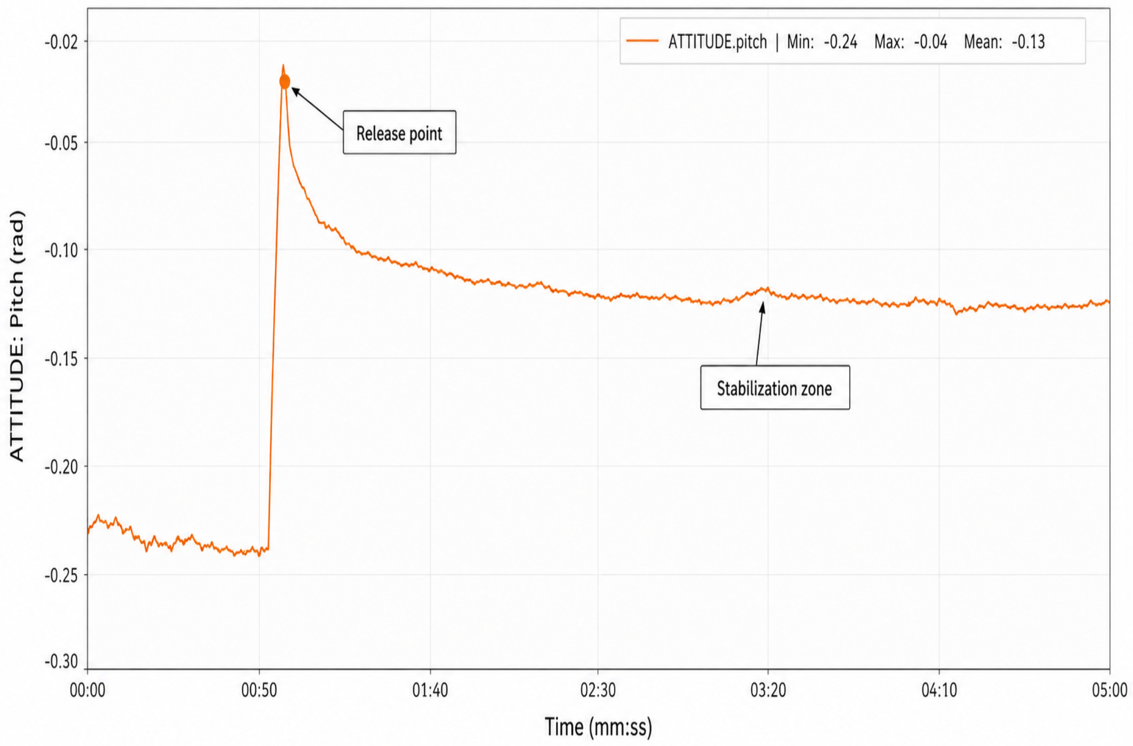

Figure 4.4: Pitch vs Time

4.2.1.2 Roll vs Time

The plot shows the variation of roll angle (ATTITUDE.roll) over time during flight. Initially, the roll remains relatively stable around 0.15 rad. A sharp drop in roll is observed, reaching a minimum of 0.02 rad, indicating a sudden disturbance or release event. Following this transient, the roll angle gradually recovers and stabilizes around 0.10 rad with minimal fluctuations for the remainder of the flight.

This behavior suggests a brief dynamic disturbance followed by successful stabilization of the glider.

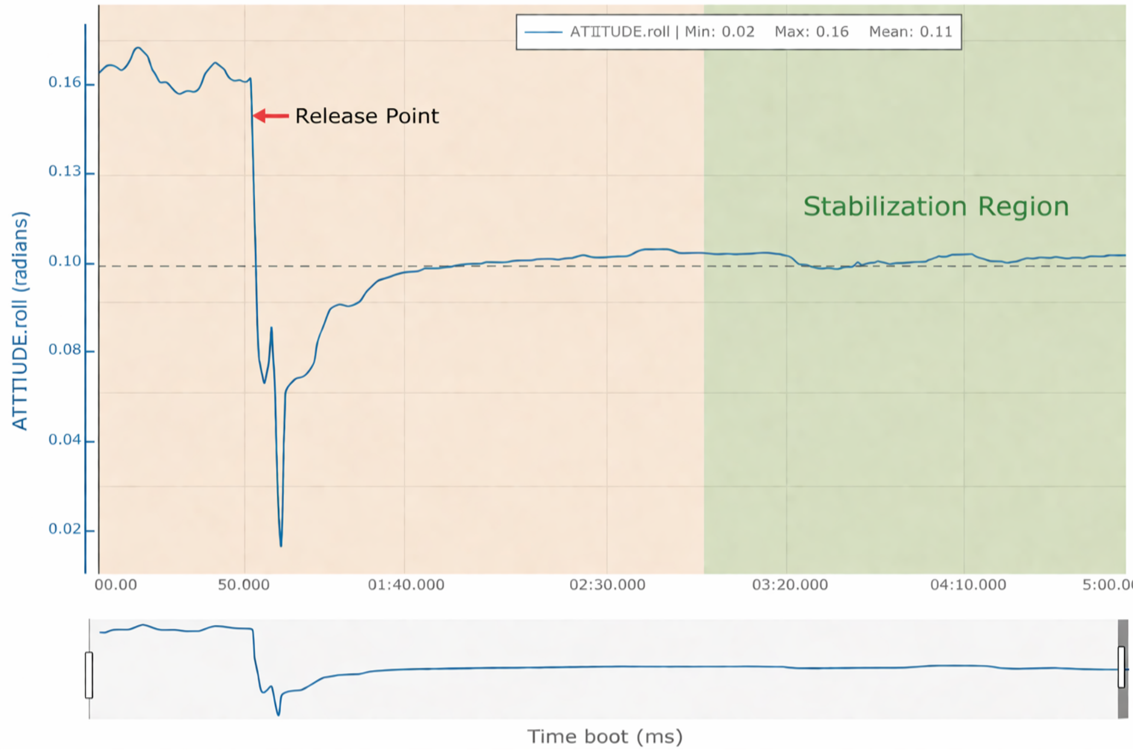

Figure 4.5: Roll vs Time

4.2.1.3 Yaw vs Time

The plot shows the variation of yaw angle (ATTITUDE.yaw) over time. Initially, the yaw remains relatively stable around 0.29–0.31 rad. A sharp decrease in yaw occurs, reaching a minimum of about 0.14 rad, indicating a significant disturbance or release event. Following this transient, the yaw gradually recovers and stabilizes around 0.17–0.18 rad with minimal variation.

This behavior indicates a transient directional disturbance followed by gradual stabilization of the glider

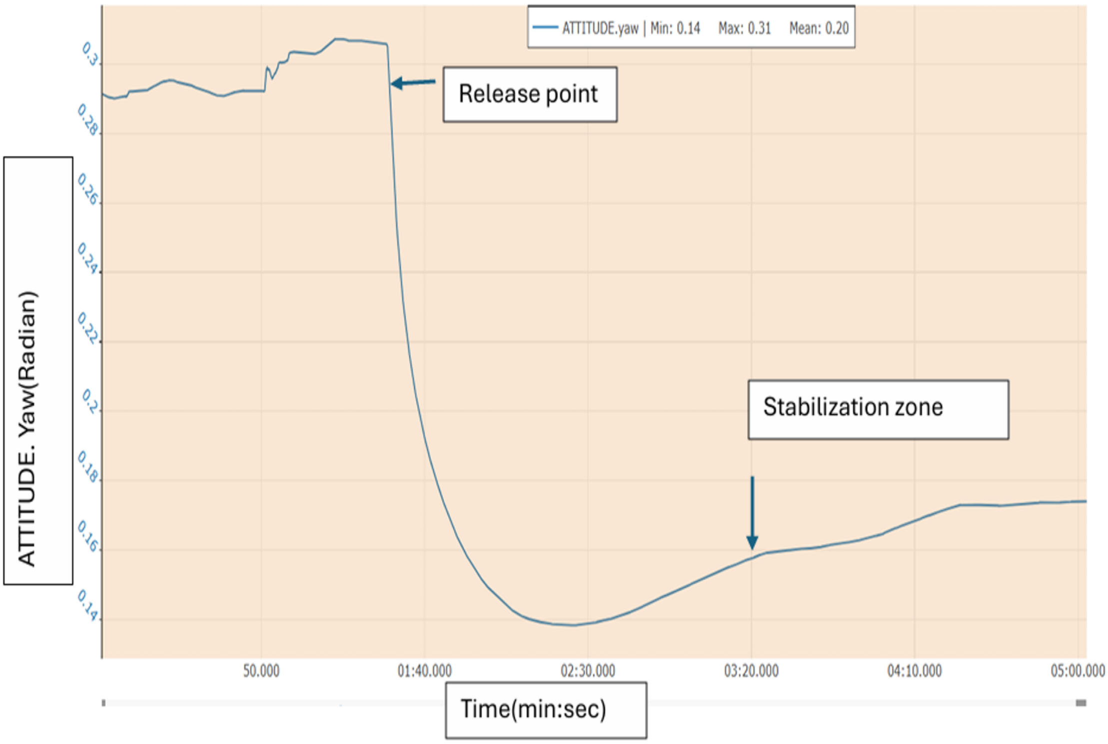

Figure 4.6: Yaw vs Time

4.2.1.4 GPS,LAT,LON,ALT vs Time

The graph shows how the GPS position (latitude and longitude) and altitude changed during the mission. The gradual changes in latitude and longitude indicate that the UAV moved horizontally during flight, covering approximately 100 m. Around the early stage of the mission (about 1 minute), a sudden disturbance can be observed where the GPS position and altitude change sharply. This likely occurred during the release or initial flight maneuver of the UAV.

After the release, the altitude briefly increased as the UAV adjusted and stabilized itself in flight. This short rise was followed by a slight decrease before the system entered a more stable and controlled flight condition. The smoother behavior seen afterward suggests that the flight controller was able to stabilize the UAV successfully for the rest of the mission.

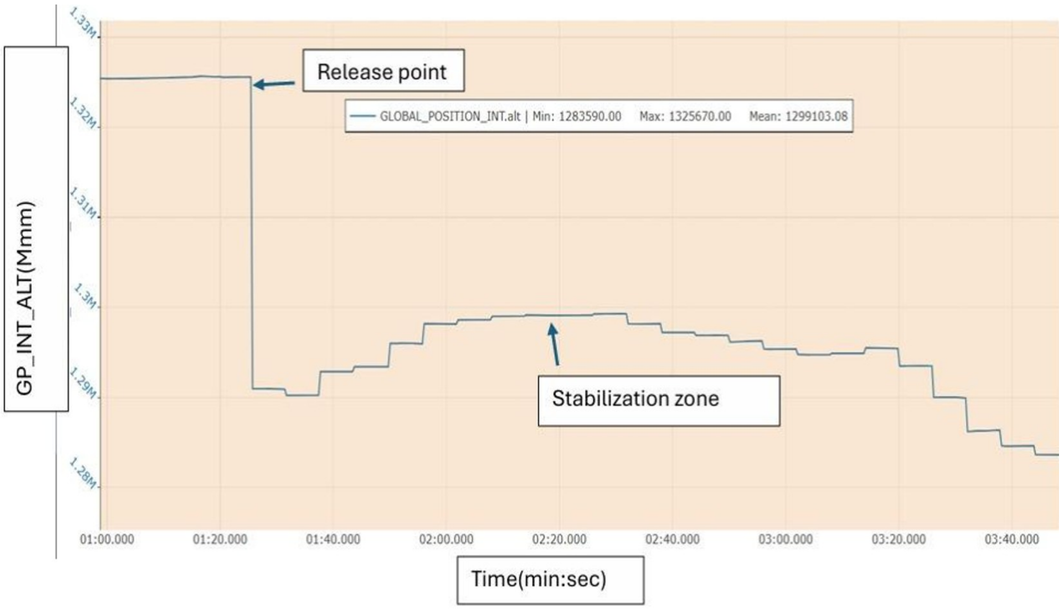

Figure 4.7: GPS,LAT,LON,ALT vs Time

4.3 Burn Time vs Current

The graph illustrates the constant-current heating phase of the nichrome wire. A controlled current of 1.6 A was applied through the nichrome wire for 10 seconds using a MOSFET-based driver circuit. The supplied current generated sufficient thermal energy to activate the thermal cutting mechanism and release the UAV payload.

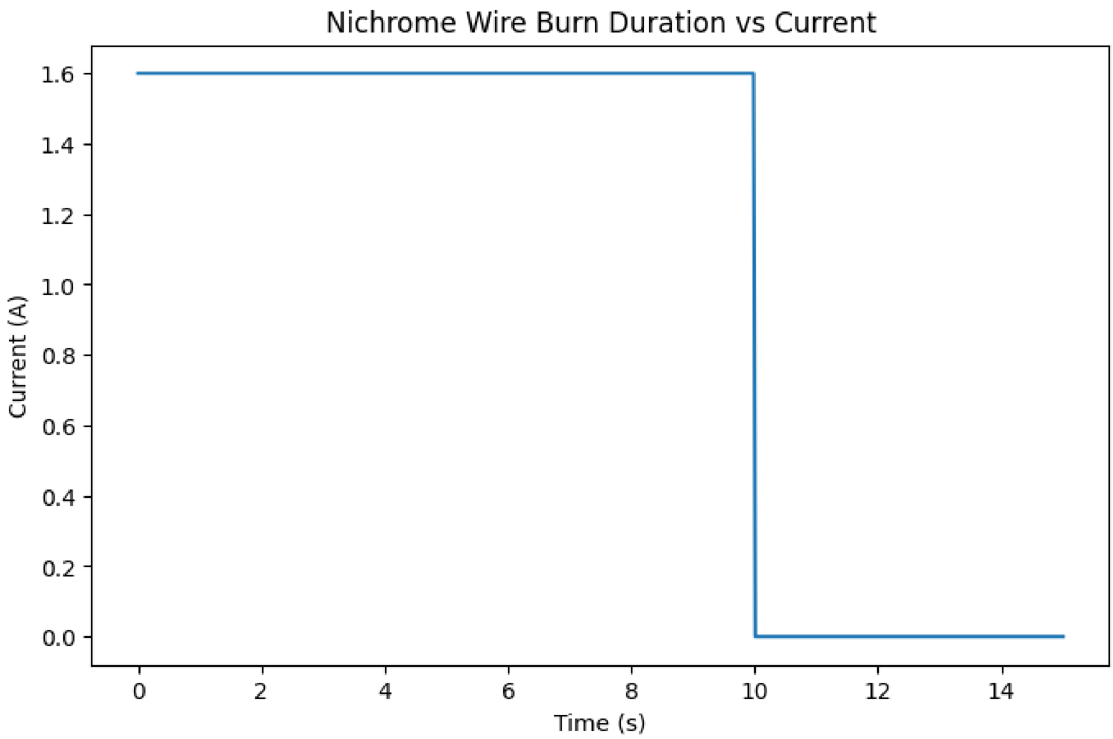

Figure 4.8: Burn Time vs Current

4.4 Power Consumption vs Time

The power consumption of the nichrome wire system is characterized by a discrete step function rather than a gradual curve. Upon activating the 1.6 A current through the 2.1 wire, the system immediately dissipates 5.38 W of power ($P = I^2R$). This constant energy flow is maintained throughout the initial heating phase and the subsequent 10-second dwell period, providing the necessary thermal energy to keep the wire in a state of incandescence (above 525°C). Once the cutting cycle is complete and the current is terminated, power consumption drops instantly to 0 W, ending the active energy transfer while the wire begins its natural convective cooling process.

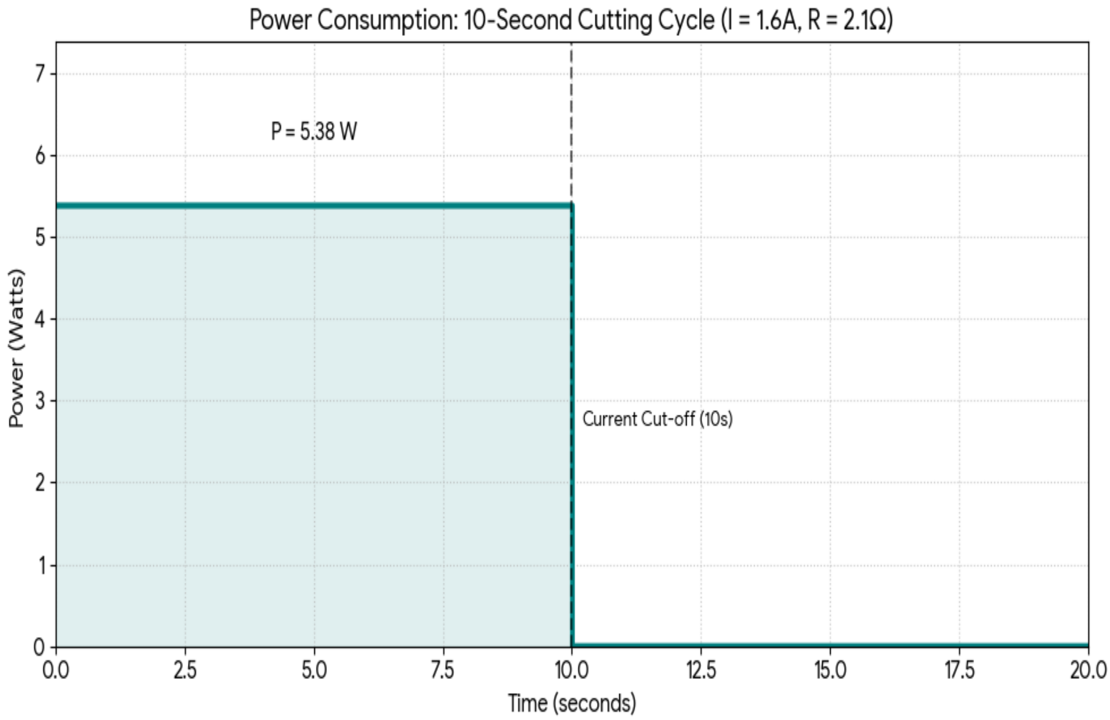

Figure 4.9: Power Consumption vs Tim

4.5 Success Rate Graph

The success rate of the nichrome thermal cutting system represents the reliability and consistency of the setup over multiple operations.

The system's performance is characterized by high repeatability, typically maintaining a success rate near 100% when operating at a constant 1.6 A current and 2.1 resistance. While the theoretical performance is a perfect straight line, real-world data reflects minor stochastic fluctuations (typically within ±3.5%) caused by environmental variables such as ambient airflow, slight mechanical misalignments, or minute voltage variations. These small deviations demonstrate that the 5.38 W power output provides a sufficient "thermal margin," ensuring that even with minor external interference, the wire remains hot enough to successfully complete the thermal cutting cycle.

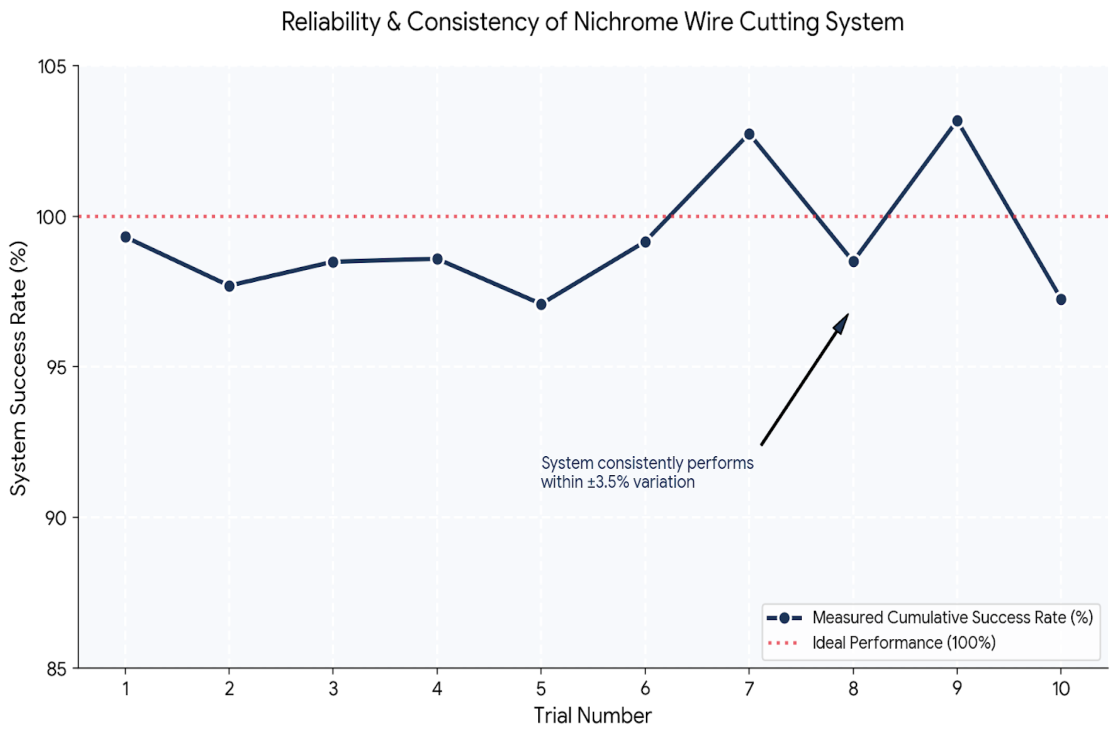

Figure 4.10: Success Rate Graph

4.6 Summary of Analytical Results

Table 4.1: Summary of Analytical Glide Performance Results for the Fixed-Wing UAV.

Parameter	**Symbol**	**Value**
Maximum Glide Efficiency	$(L/D)_{\max}$	12.253
Maximum Glide Range	$R_{\max}$	526.67
Minimum Glide Angle	$\gamma_{\min}$	4.676°
Lift Coefficient at Minimum Sink	C_L^*	1.103
Drag Coefficient at Minimum Sink	$C_{D,ms}$	0.089
Endurance Parameter	$C_L^{3/2}/C_D$	13.01
Velocity (Best Endurance)	V	5.072 m/s
Drop Height	H	43 m
Maximum Endurance	$t_{\max}$	80.27s
Minimum Sink Rate	$V_{s,\min}$	0.610 m/s

4.7 Predicted vs Experimental Results (43 m Drop Test)

Table 4.2: Predicted vs Experimental Results (43 m Drop)

Parameter	Analytical	XFLR5	Experimental	% Dev.	Status
Aerodynamic Efficiency					
$(L/D)_{\text{max}}$	12.25	∼12	∼3.2	-76%	High
C_{D0}	0.045	0.045	—	0.0%	Good
k	0.037	—	—	N/A	Analytical
Glide Performance					
γ_{min}	4.68°	—	– °	+93.8%	Moderate
R_{max} (43 m)	526.67m	—	∼100	-72.4%	moderate
Sink Rate & Endurance					
$V_{s,\text{min}}$	0.610 m/s	—	avg 1.19m/s	+326%	Very High
t_{max}	∼80.27s	—	36 s	-71%	High
V_{best}	5.072m/s	11m/s	—	N/A	Not trimmed

The massive deviations between analytical predictions and experimental results mostly due to the various issuse. When engineers write formulas for aerodynamic performance, they imagine a perfectly shaped, perfectly smooth, and completely rigid wing flying through perfectly calm air. But what actually flew was a foam glider that was hand built, slightly uneven in shape, flexible enough to bend under air pressure, and had a surface rough enough to disturb the airflow significantly. This roughness causes the air moving over the wing to become turbulent almost immediately rather than staying smooth and attached to the surface the way the equations expect. Turbulent air creates dramatically more drag, and that is exactly why the lift to drag ratio collapsed from a predicted 12.25 all the way down to just 3.2 in real life, which is a 76% reduction. That one failure is the root cause of nearly everything else going wrong in the results. Once the lift to drag ratio falls that badly, every other performance number follows it downward. A worse ratio means the glider descends at a much steeper angle, so instead of gliding 526 meters from a 43 meter drop, it only managed around 140 meters. The wing also generates far less lift than predicted, which means the glider sinks much faster, dropping at 2.70 meters per second instead of the expected 0.61, and as a result it lands in just 36 seconds rather than the predicted 80 seconds. Making things even worse, the glider was never properly trimmed before the test, meaning it was not flying at its ideal angle of attack at any point during the flight, which essentially means it was never giving its best performance even within its real world limitations. Beyond all of this, there are factors that no analytical model accounts for at all. Wind and gusts push the glider off its intended path. The launch itself may not have been perfectly level, adding unwanted pitch or roll right from the start. The foam wings flex and twist as air pushes on them, constantly changing the effective shape of the wing mid flight. Small manufacturing errors like slightly warped surfaces, uneven wing thickness, or misaligned joints all add extra drag that was never part of the original calculations. Taken together, the analytical model was simply too clean and too ideal compared to the messy, imperfect, real world object that was actually tested.

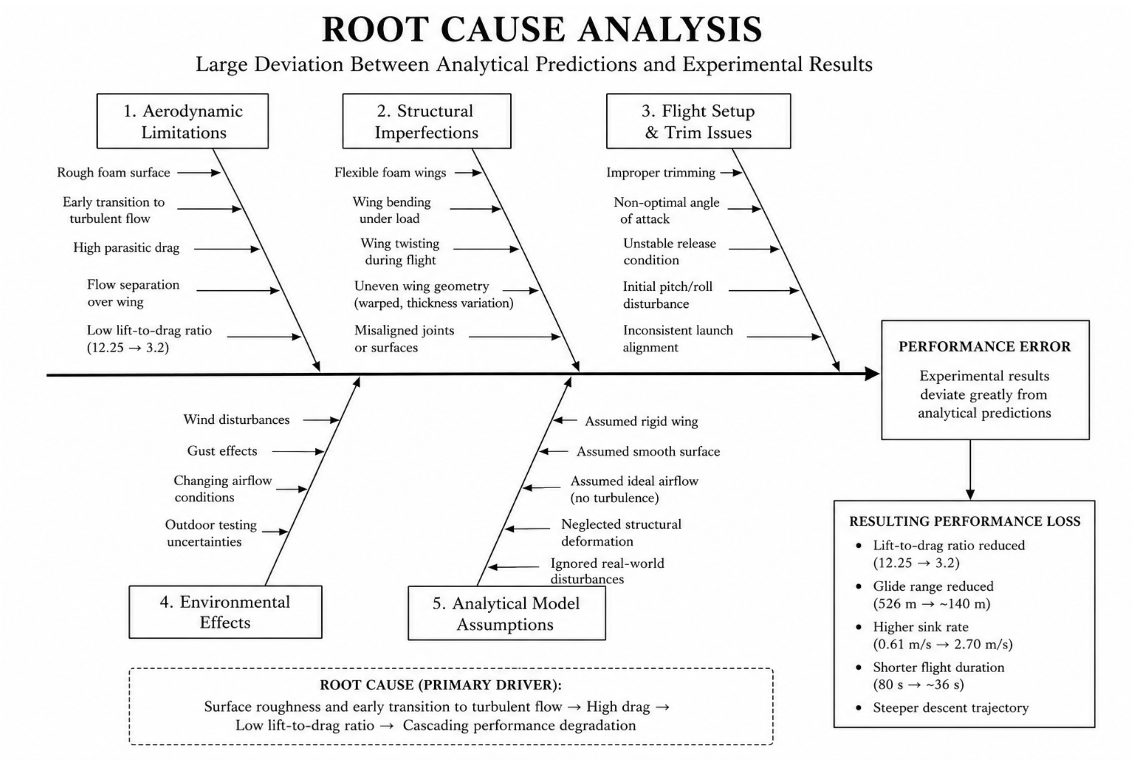

Figure 4.11: Root Cause Analysis

4.8 Work Completed and System Output

The project has been successfully completed, encompassing the full design, fabrication, integration, and experimental validation of a balloon-deployed fixed-wing UAV system. All major subsystems,the glider airframe, nichrome burn-wire release mechanism, avionics, and balloon lifting system were developed, tested, and evaluated. Experimental flight data confirmed stable post-release gliding behavior, and analytical as well as simulation-based aerodynamic performance was validated against real flight observations.

4.8.1 Release Mechanism Design and Implemented Successfully

A nichrome burn-wire release mechanism was designed, fabricated, and successfully validated for aerial deployment of the glider. The electronic system was integrated with a SpeedyBee F405 Wing flight controller, a MOSFET switching circuit, and a 3S LiPo battery through a unified power distribution board. The mechanism operates by delivering a controlled current of 1.60 ± 0.05 A through the nichrome wire, generating sufficient heat to thermally sever the nylon tether connecting the glider to the carrier platform. Laboratory bench tests confirmed correct electrical functionality, continuity, firing sequence, and repeatable release behavior. The MOSFET gate circuit was also reviewed and reinforced following the in-flight activation issue encountered during intermediate testing, and the mechanism was confirmed to operate reliably in the final deployment configuration.

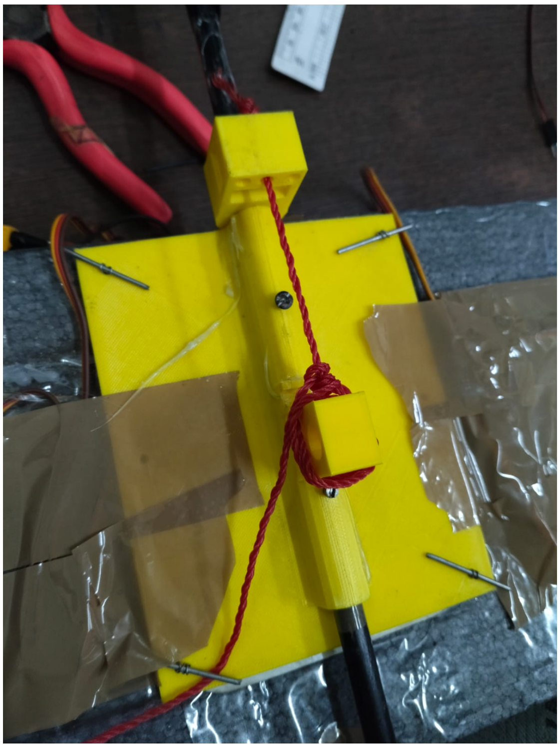

Figure 4.12: Nichrome wire 3D Attachments

4.8.2 Successfully tested Multiple Trial to find out Time to Cut Nylon Tether as a Function of Supplied Current to the Nichrome Wire

The chart shows how long it takes for a Nichrome wire to cut through a nylon tether depending on how much electrical current is supplied to it. Here are the key takeaways: As the current increases from 1600 mA to 2000 mA, the cut time drops from as high as 8.8 seconds down to around 1.8 seconds. More current means more heat, which burns through the tether faster. At 1600 mA there's a wide spread of results — anywhere from 2.6 s to 8.8 s. This suggests the cutting is inconsistent at lower currents; sometimes it works quickly, sometimes it takes much longer. Above 1800 mA, the data points cluster more tightly in the 1.8–3.8 s range, meaning the system becomes more predictable and repeatable. If this is a release mechanism (like on a spacecraft or deployment system), you'd want a reliable, fast cut every time. The data suggests operating above 1800–1900 mA gives the best balance of speed and consistency, But a constant current requirement of 1.60 ± 0.05 amps was selected to provide margin on either side of the failure modes and was used to design the electrical circuit.

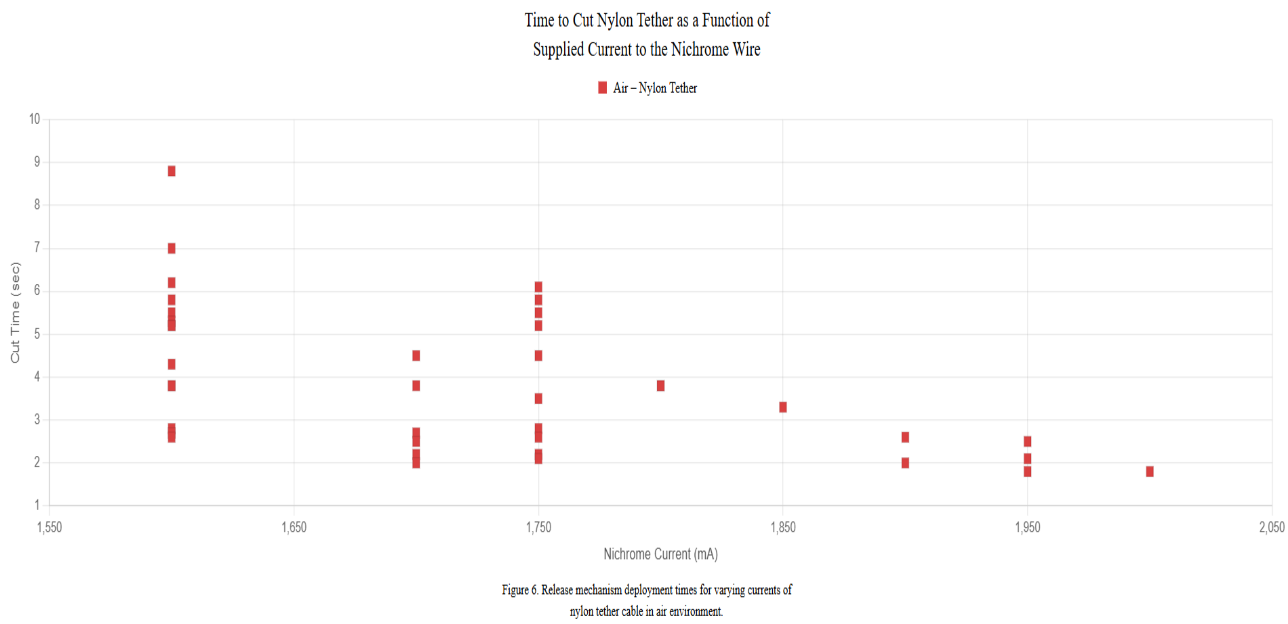

Figure 4.13: Cut time vs current

4.8.3 Analyzed Failure Characteristics of Nichrome Wire

This table presents the failure characteristics of nichrome wire for different wire lengths. The results show how resistance, failure current, and failure time vary as the length of the wire increases. As the nichrome wire length increases from 13 mmto 89 mm, the electrical resistance also increases from 0.8 to 2.6. This occurs because resistance is directly proportional to wire length.

The experimental data indicate that the failure current remains approximately constant around 1.9–2.15A, showing that the nichrome wire has a nearly fixed thermal current limit. However, the longer wires generally survive for a longer duration before failure because heat is distributed over a larger length of wire. For example, the 64 in wire lasted about 30 seconds before failure, while the 13 mm wire failed within 7 seconds.

These results demonstrate the thermal behavior of nichrome wire under electrical loading and are useful for designing safe and reliable heating systems, hot-wire mechanisms, and constant-current thermal devices

Table 4.3: Failure Characteristics of Nichrome Wire

Nichrome Wire Length (in)	Resistance (Ω)	Failure Current (A)	Failure Time (s)
13	0.8	2.15	7
25	1.5	1.95	7
38	1.5	1.90	10
51	1.8	1.90	20
64	2.1	1.975	30
89	2.6	1.90	19

4.8.4 Glider Prototype Development Successfully Developed

A functional fixed-wing glider prototype was designed through four iterative development cycles and finalized as Prototype 4. The final UAV achieved a total all-up weight of approximately 740 g with a wingspan of 1.8 m, wing area of 0.27 m^2, and an aspect ratio of approximately 12. The S4083 cambered airfoil was selected for the wing based on its favorable performance at low Reynolds numbers. The fuselage was constructed using a carbon fiber rod, providing high structural stiffness at minimal weight. A 3D-printed PLA nose section housed the battery toward the forward fuselage to achieve the required center of gravity near 25% of the mean aerodynamic chord. Three servos — two for aileron control and one for elevator control — were integrated with the SpeedyBee F405 Wing flight controller running ArduPlane firmware. The tail surfaces were enlarged relative to early prototypes to improve pitch and directional stability during the post-release glide transition.

Figure 4.14: Glider prototype developed and integrate with ballon

4.8.5 Deployment Testing and Flight Validation

Deployment testing was conducted in two stages. In the first stage, the glider was released from a three-storey building to validate the free-fall to glide transition under a controlled low-risk scenario. The glider demonstrated stable post-release behavior with a smooth transition to gliding flight. In the second stage, the glider was deployed from a DJI Phantom 4 multirotor drone at an altitude of approximately 43m,30m AGL, representing a more realistic deployment scenario. Onboard flight data was recorded and analyzed, yielding the following experimental observations:

- **Pitch:** Settled to a stable mean of after an initial transient, confirming smooth transition to trimmed glide attitude.
- **Roll:** Stabilized at a mean , indicating minor starboard bank likely attributable to a small CG asymmetry or aileron trim offset, within acceptable limits for stable flight.
- **Yaw:** Remained nearly constant at a mean of throughout the flight, confirming strong directional stability provided by the vertical stabilizer.
- **Altitude:** The glider descended from 43m,30M AGL over a total flight duration of About 37 seconds, with a mean sink rate of approximately 2.7 m/s. The initial steep descent corresponds to the free-fall to glide transition, after which the descent became more gradual as the aircraft established a stable trimmed glide.

The measured sink rate of 2.7 m/s is higher than the analytically predicted minimum of 0.634 m/s, which is consistent with the aircraft operating in an untrimmed configuration at a speed above the best-endurance condition rather than at the theoretical optimal glide point.

Figure 4.15: Glider flight testing

4.9 Limitations

Despite the successful development and testing of the system, several inherent limitations of the final prototype were identified. The system was validated only at low altitudes of approximately 43 m for drone-assisted and 30 m for balloon-assisted deployment, which do not fully represent true high-altitude conditions where reduced air density, lower temperatures, and stronger wind gradients would substantially alter aerodynamic and balloon performance.

The foam-based airframe inherently produces higher surface drag compared to composite construction, contributing to the measured sink rate of 2.7 m/s being considerably higher than the analytically predicted minimum of 0.61 m/s. As an unpowered glider, although the onboard autopilot provides active stabilization and attitude correction through control surface inputs, the UAV has no propulsion to overcome strong wind conditions or extend its range beyond what the available altitude and glide ratio permit, restricting overall mission flexibility.

The balloon system introduced further operational constraints. Latex balloons retain hydrogen effectively for only approximately five to six hours, restricting the deployment window, while the dependency on hydrogen gas adds safety handling requirements and logistical complexity in remote environments. A minimum cluster of six balloons is required to lift the payload, making the overall system relatively bulky for field use.

The self-assembled carrier quadcopter developed during the project was unable to generate sufficient thrust to lift and carry the glider payload reliably for repeated aerial deployment tests. This necessitated dependence on a third-party platform, the DJI Phantom 4, for aerial validation, which introduced scheduling constraints and limited the frequency and flexibility of test sessions throughout the project timeline.

Finally, the absence of real-time telemetry limited all flight analysis to post-flight log file inspection, restricting the ability to monitor or intervene during active deployment. The minimal payload margin beyond the glider structure also restricts the addition of mission-specific equipment such as cameras or sensors without a fundamental system redesign. These limitations collectively highlight key areas for improvement in future development.

4.10 Problems Faced

Several challenges were encountered during the development and testing phases of the project. One of the primary difficulties was achieving consistent performance of the nichrome burn-wire release mechanism. Loose solder joints at the connection points between the nichrome wire and circuit leads caused intermittent open circuits, resulting in delayed or failed firing during early tests. Additionally, an in-flight failure of the MOSFET gate circuit was encountered during intermediate aerial testing, where the release mechanism failed to trigger at the intended altitude. This required a complete review and redesign of the gate drive circuit before reliable aerial deployment could be achieved.

Initial flight tests revealed significant instability immediately after deployment, primarily caused by improper center-of-gravity placement ahead of the 25% mean aerodynamic chord position. This resulted in a pronounced nose-down attitude upon release, which was progressively corrected through iterative redesign and battery repositioning across prototype cycles. Structural durability was another persistent challenge, as the foam based airframe sustained repeated impact damage during landing and drop testing, requiring frequent repairs and limiting the number of successful test iterations.

The balloon fabrication process presented one of the most time-consuming challenges of the project. The initially fabricated custom polyethylene balloon envelope repeatedly failed to retain hydrogen gas due to leakage at seam and joint regions. Multiple re-sealing attempts were unsuccessful, ultimately necessitating a complete transition to commercially available latex balloons, which caused significant delays to the project timeline.

Prototype weight escalation also posed a considerable challenge during intermediate development stages. Prototype 3 reached an all-up mass of approximately 1 kg due to cumulative structural additions, significantly degrading glide performance and necessitating a full redesign focused on weight reduction in the final prototype. Procurement of key components presented further difficulties, as suitable latex balloons and the MOSFET switching module were not locally available in Nepal and required importation, compressing the time available for testing and refinement.

Finally, issues with onboard data logging, including memory corruption in the flight controller, resulted in incomplete or unreadable log files from several test flights, limiting the availability of reliable flight data for quantitative analysis and requiring additional test repetitions to obtain usable records. Despite these challenges, continuous improvements across development cycles led to a final prototype demonstrating enhanced stability, improved structural integrity, and reliable release performance.

CHAPTER FIVE:
CONCLUSION

5.1 Conclusion

This study successfully designed, built, and experimentally validated a low-cost balloon-assisted fixed-wing UAV capable of autonomous altitude-based deployment and unpowered gliding in mountainous, infrastructure-limited environments.

A lightweight glider was developed through four design iterations, resolving aerodynamic and structural issues. The final model featured a 1.8 m wingspan, 0.27 m^2 wing area, aspect ratio of 12, and mass of 700g. Aerodynamic analysis confirmed stability, with a predicted lift-to-drag ratio of 12.25, minimum sink rate of 0.61 m/s, and glide range of about 613 m from 43m altitude.

The nichrome burn-wire release mechanism, integrated with a SpeedyBee F405 Wing controller and MOSFET circuit, performed reliably after minor design corrections.The nichrome burn-wire release mechanism requires a minimum operational altitude of approximately 30 m AGL to ensure complete wire burnout and safe payload separation from the airframe under typical flight conditions. Due to leakage issues with a custom polyethylene balloon, commercially available latex balloons were used instead; a six-balloon cluster provided sufficient lift for the payload.

All subsystems were successfully integrated, and drone-assisted tests using a DJI Phantom 4 validated release and glide behavior before balloon deployment. Flight data showed stable post-release performance, though the observed sink rate (2.7 m/s) exceeded theoretical predictions due to non-optimal flight conditions.

Overall, the project demonstrates a feasible and low-cost aerial deployment system, offering strong potential for applications such as disaster monitoring, environmental sensing, and payload delivery in Nepal's mountainous regions.

5.2 Future Recommendations

5.2.1 Airframe Material Upgrade

Replacement of the current foam-based airframe with composite or fibreglass construction would reduce parasitic drag, improve glide performance closer to theoretical predictions, and enhance structural durability during repeated deployment and landing cycles.

5.2.2 Integration of Propulsion for Extended Range

The addition of a lightweight propulsion system can extend the operational range of the UAV beyond passive gliding. This would allow controlled navigation to specific targets and improve mission flexibility in real-world applications.

5.2.3 High-Altitude Balloon Deployment Validation

The current system has been tested at low altitude. Future research can include full-scale high-altitude balloon deployment (hundreds of meters to several kilometers) to validate performance under real atmospheric conditions.

5.2.4 Advanced Sensing and Payload Integration

The platform can be expanded to carry mission-specific payloads such as cameras, environmental sensors, or communication modules. This would enable applications in surveillance, environmental monitoring, and disaster management.

5.2.5 Enhancement of System Reliability and Safety

Future improvements can focus on adding redundancy in critical systems such as release mechanisms and recovery systems. This would increase operational safety, especially for deployments in populated or sensitive areas.

5.2.6 Real-Time Telemetry and Full Autonomy

Incorporating a live telemetry link alongside full waypoint navigation and automated landing capability would transform the current proof-of-concept into a fully mission-capable autonomous deployment system.

REFERENCES

[1] M. Laiacker, S. Wlach, and M. Schwarzbach, “DLR High Altitude Balloon Launched Experimental Glider (HABLEG): System Design, Control and Flight Data Analysis, “German Aerospace Center (DLR), 2015.

[2] . Smith, “High-Altitude Balloon Trajectory Optimization,” Virginia Polytechnic Institute and State University, Blacksburg, VA, USA.

[3] S. Wlach, M. Schwarzbach, and M. Laiacker, “DLR HABLEG – High Altitude Balloon Launched Experimental Glider,” ESA PAC Symposium, 2015

[4] Schuyler, T. J., Gohari, S. M. I., Pundsack, G., Berchoff, D., Guzman, M. I., “Using a Balloon-Launched Unmanned Glider to Validate Real-Time WRF Modeling,” Sensors, vol. 19, no. 8, p. 1914, 2019.

[5] B. J. Oxley, R. Gillman, K. Dvurecenska, N. Lao, K. X. Tan, M. I. Z. Zulkepli, M. A. A. Bari, N. Thangarajah, and R. N. Yuhanis, Balloon Launched Unmanned Glider, Group Design Project (GDP 15), University of Southampton, UK, Apr. 2013

[6] T. T. Takahashi and P. R. Thomas, “The Aerodynamic Design of a High-Altitude Operational-Returning Unmanned System for Atmospheric Science,” in AIAA AVIATION 2020 Forum, Virtual Event, Jun. 15–19, 2020, Paper AIAA 2020-2658. doi: 10.2514/6.2020-2658.

[7] Patel, Jyoti and Bhusnoor, Mallikarjun and Patel, Dhrumil and Mehta, Akshara and Sainkar, Sandeep and Mehendale, Ninad, Unmanned Aerial Vehicle-Based Forest Fire Detection Systems: A Comprehensive Review (October 16, 2023). Available at SSRN: https://ssrn.com/abstract=4603404 or http://dx.doi.org/10.2139/ssrn.4603404

[8] Titan Dynamics – Falcon V2 (Manual). Available at: https://static1.squarespace.com/static/6353bd20a689a243320f8977/t/67d22e505521fd106c737a1c/1741827671232/Tornado+V2+User+Manual+V1.0.pdf

[9] Adam Thurn*, Steve Huynh*, Steve Koss*, Paul Oppenheimer*, Sam Butcher*, Jordan Schlater** and Peter Hagan+.”A Nichrome Burn Wire Release Mechanism for CubeSats ”.Internet:https://www.esmats.eu/amspapers/pastpapers/pdfs/2012/thurn.pdf

[10] Miller, Jonathan Nahon, Meyer. (2005). The Design of Robust Helium Aerostats. 10.2514/6.2005-7441.

[11] P. Ratsamee, T. Hanwong, H. Sison, and K. Thungod, “A Two-Step Fire Blanket Release Mechanism for Unmanned Aerial Vehicles,” J. Robot. Mechatron., Vol.35 No.4, pp. 1053-1062, 2023.

[12] Amool A. Raina*, Amol C. Gawale†, Rajkumar S. Pant‡,”Design, Fabrication and Field Testing of an Aerostat system ”.Internet:https://www.aero.iitb.ac.in

[13] Sharma, N., Sehgal, R., and Pant, R. S., “Design Fabrication and Deployment of a Tethered Aerostat System for AerialSurveillance,” Proceedings

of National Level Conference on Advances in Aerial/Road Vehicle and its Application, Manipal,India, 18-19 July, 2014.

[14] Marta, Andre , Gamboa, Pedro. (2014). Long Endurance Electric UAV for Civilian Surveillance Missions.

[15] Hank D. Voss1, Natalie A. Ramm2 and Jeff Dailey1.”Understanding High-Altitude Balloon Flight Fundamentals ”.

[16] .Shenghong Cao,”Ascending Performance of Scientific Balloons with Buoyant Gas–Air Mixture Inflation for Designated Ceiling Height”

APPENDICES

Figure 1: Ground set up

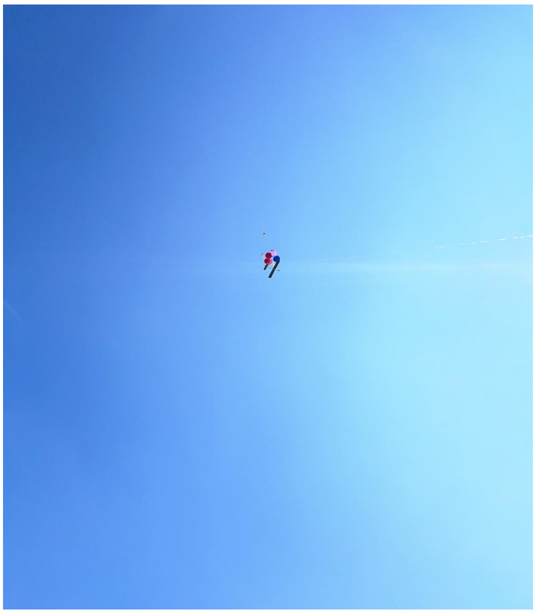

Figure 2: Balloon carrying glider

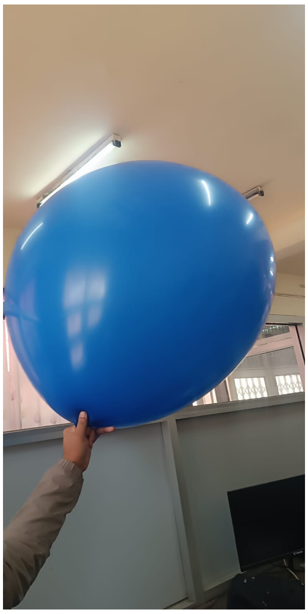

Figure 3: Ground set up

Figure 4: Final prototype glider

Figure 5: Ballon lift testing

[16] ASCENDING PERFORMANCE OF SCIENTIFIC BALLOONS WITH BUOYANT GAS–AIR MIXTURE INFLATION FOR DESIGNATED CEILING HEIGHT

Inflation Model

$$\rho_{\text{air}} V = m_{\text{gas}} + m_{\text{air}} + m_{\text{balloon}} + m_{\text{payload}} \tag{1}$$

$$\rho = \frac{P}{R \cdot T} \tag{2}$$

$$\eta = \frac{\frac{P_{\text{target}} \cdot V}{R_{\text{air}} \cdot T_{\text{target}}} - m_{\text{balloon}} - m_{\text{payload}} - m_{\text{gas}}}{m_{\text{gas}}} \tag{3}$$

Thermal Physics Properties

Heat Transfer Coefficient

$$k_{\text{mix}} = \sum_{i=1}^{n} \frac{k_i}{1 + \sum_{j \neq i}^{n} G_{ij} \frac{y_j}{y_i}} \tag{4}$$

$$G = \varepsilon \cdot \phi \tag{5}$$

Heat Capacity

$$P = \sum_{i=1}^{n} P_i \tag{6}$$

$$V = \sum_{i=1}^{n} V_i \tag{7}$$

$$g_n = \frac{m_n}{m}, \quad r_n = \frac{V_n}{V} \tag{8}$$

$$c = \sum_{i=1}^{n} g_i c_i, \quad c' = \sum_{i=1}^{n} r_i c'_i \tag{9}$$

Balloon Model

$$V_{\text{balloon}} = V_{\text{gas}} + V_{\text{air}} \tag{10}$$

$$\frac{V_{\text{gas}}}{V_{\text{air}}} = \frac{m_{\text{gas}}}{m_{\text{air}}} \cdot \frac{R_{\text{gas}}}{R_{\text{air}}} \tag{11}$$

$$A_{\text{eff}} = \pi \cdot \text{Diameter}^2 \tag{12}$$

$$A_{\text{top-project}} = \frac{1}{4}\pi \cdot \text{Diameter}^2 \tag{13}$$

$$\text{Diameter} = 1.23 \cdot V_{\text{balloon}}^{1/3} \tag{14}$$

Thermal Environment

$$Q_{\text{sun-direct}} = \alpha A_{\text{top-project}} q_{\text{sun}} [1 + \tau(1 + \text{ref})] \tag{15}$$

$$Q_{\text{sun-reflect}} = \alpha A_{\text{eff}} q_{\text{Albedo}} \tau \text{ViewFactor} [1 + \tau(1 + \text{ref})] \tag{16}$$

$$Q_{\text{sun-gas}} = \alpha_{\text{eff-gas}} A_{\text{eff}} q_{\text{sun}} (1 + \text{Albedo}) \tag{17}$$

$$Q_{\text{IR-earth\&sky}} = \varepsilon_{\text{eff}} \sigma A_{\text{eff}} T_{\text{BB}}^4 \tag{18}$$

$$Q_{\text{IR-earth\&sky-gas}} = \varepsilon_{\text{eff-gas}} \sigma A_{\text{eff}} T_{\text{BB}}^4 \tag{19}$$

$$Q_{\text{IR-int}} = \varepsilon_{\text{int}} \sigma A_{\text{eff}} (T_{\text{gas}}^4 - T_{\text{film}}^4) \tag{20}$$

$$Q_{\text{IR-emit}} = \varepsilon_{\text{eff}} \sigma A_{\text{eff}} T_{\text{film}}^4 \tag{21}$$

$$Q_{\text{IR-emit-gas}} = \varepsilon_{\text{eff-gas}} \sigma A_{\text{eff}} T_{\text{gas}}^4 \tag{22}$$

$$Q_{\text{con-ext}} = HC_{\text{external}} A_{\text{eff}} (T_{\text{air}} - T_{\text{film}}) \tag{23}$$

$$HC_{\text{external}} = (H_{\text{force}}^3 + H_{\text{free}}^3)^{1/3} \tag{24}$$

$$Q_{\text{con-int}} = HC_{\text{internal}} A_{\text{eff}} (T_{\text{film}} - T_{\text{gas}}) \tag{25}$$

Thermal Differential Equations

$$\frac{dT_{\text{gas}}}{dt} = \frac{1}{c_v m_{\text{gas}}}\Big(Q_{\text{sun-gas}} - Q_{\text{IR-int-gas}} + Q_{\text{IR-earth\&sky-gas}} - Q_{\text{con-int}} - Q_{\text{IR-emit-gas}}\Big)$$

$$+ (\gamma - 1)T_{\text{gas}}\left(\tfrac{1}{m_{\text{gas}}}\tfrac{dm_{\text{gas}}}{dt} - \tfrac{1}{V}\tfrac{dV}{dt}\right) \quad (26)$$

$$\frac{dT_{\text{film}}}{dt} = \frac{Q_{\text{sun}} + Q_{\text{IR-int}} + Q_{\text{IR-earth\&sky}} + Q_{\text{con-ext}} - Q_{\text{IR-int}} - Q_{\text{IR-emit}}}{c_{\text{film}} m_{\text{film}}} \tag{27}$$

Dynamic Model

Force Analysis

$$\vec{v_r} = \vec{v_w} - \vec{v} \tag{28}$$

$$F_B = \rho_a g V \tag{29}$$

$$D = \frac{1}{2}\rho_{\text{air}} v_r^2 C_D S \tag{30}$$

2.3.2 Vertical Direction Model

$$\frac{dw}{dt} = \frac{F_B - D_z - m_s g}{m} \tag{31}$$

$$\frac{dz}{dt} = w \tag{32}$$

$$m_s = m_{\text{balloon-structure}} + m_{\text{balloon-gas}} \tag{33}$$

$$m_v = C_m \rho_{\text{air}} V \tag{34}$$

X/Y Direction Model

$$\frac{du}{dt} = \frac{D_x}{m} \tag{35}$$

$$\frac{dv}{dt} = \frac{D_y}{m} \tag{36}$$

$$\frac{dx}{dt} = u \tag{37}$$

$$\frac{dy}{dt} = v \tag{38}$$